# Influence of the Ligand Field on the Slow Relaxation of Magnetization of Unsymmetrical Monomeric Lanthanide Complexes: Synthesis and Theoretical Studies

Apoorva Upadhyay, Kuduva R. Vignesh, Chinmoy Das, Saurabh Kumar Singh, Gopalan Rajaraman,* and Maheswaran Shanmugam*

Department of Chemistry, Indian Institute of Technology Bombay, Powai, Mumbai, Maharashtra 400076, India

S Supporting Information

ABSTRACT: A series of monomeric lanthanide Schiff base complexes with the molecular formulas $[Ce(HL)_3(NO_3)_3]$ (1) and $[Ln(HL)_2(NO_3)_3]$, where Ln^{III} = Tb (2), Ho (3), Er (4), and Lu (5), were isolated and characterized by single-crystal X-ray diffraction (XRD). Single-crystal XRD reveals that, except for 1, all complexes possess two crystallographically distinct molecules within the unit cell. Both of these crystallographically distinct molecules possess the same molecular formula, but the orientation of the coordinating ligand distinctly differs from those in complexes 2−5. Alternating-current magnetic susceptibility measurement reveals that complexes 1−3 exhibit slow relaxation of magnetization in the presence of an optimum external magnetic field. In contrast to 1−3, complex 4 shows a blockade of magnetization in the absence of an external magnetic field, a signature characteristic of a single-ion magnet (SIM). The distinct magnetic behavior observed in 4 compared to other complexes is correlated to the suitable ligand field around a prolate Er^{III} ion. Although the ligand field stabilizes an easy axis of anisotropy, quantum tunnelling of magnetization (QTM) is still predominant in 4 because of the low symmetry of the complex. The combination of low symmetry and an unsuitable ligand-field environment in complexes 1−3 triggers faster magnetization relaxation; hence, these complexes exhibit field-induced SIM behavior. In order to understand the electronic structures of complexes 1−4 and the distinct magnetic behavior observed, ab initio calculations were performed. Using the crystal structure of the complexes, magnetic susceptibility data were computed for all of the complexes. The computed susceptibility and magnetization are in good agreement with the experimental magnetic data $[\chi_M T(T)$ and $M(H)]$ and this offers confidence on the reliability of the extracted parameters. A tentative mechanism of magnetization relaxation observed in these complexes is also discussed in detail.
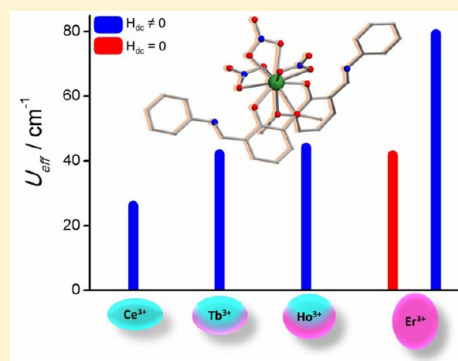
INTRODUCTION

The intrinsic orbital angular momentum associated with lanthanide ions makes them suitable candidates for the design of a single-molecule-magnet (SMM) or a single-ion magnet (SIM) compared to transition metal ion complexes.[1] Intensive research on the SMM or SIM design by various research groups has been carried out because both SMMs and SIMs encapsulate potential applications such as spintronic,[2] spin valve,[3] high density storage,[1f,4] and molecular qubits.[5] Unlike the first generation of SMM design based on transition metal complexes,[6] the ligand field around the lanthanide ion lifts the degeneracy of the m_j levels, which is responsible for the magnetization blockade in certain lanthanide complexes; hence, a suitable ligand field around the lanthanide ion can yield the desired magnetic properties.[7] An approximate D_{4d} geometry provided by the phthalocyanine ligand stabilizes an easy-axis anisotropy in $[Tb(Pc)_2]^{n-,0,n+}$ complexes showing slow relaxation of magnetization reported by Ishikawa and co-workers in 2003.[1a] Following this discovery, several lanthanide-based SIMs and SMMs flooded the literature.[1g,8] Among the SIMs and SMMs reported in the literature, the Dy^{III} ion holds

an edge over other lanthanide ions because of the Kramers nature of the m_j levels coupled with the absence of a nuclear spin moment.[1f] In majority of the lanthanide complexes, magnetic bistability arises by a conventional magnetization blockade; however, certain oligomeric lanthanide complexes show magnetic bistability due to spin chirality or single-molecule toroics[8p] and an even more fascinating phenomenon called magnetic-chiral dichroism exhibited by certain one-dimensional complexes recently reported by Sessoli and co-workers.[9]

Although a magnetization blockade is observed in a variety of transition- and lanthanide-based SMMs or SIMs, the blocking temperatures are still significantly low (<4 K) in the majority of the complexes, except a few.[10] This is due to the counterbalancing act of magnetic anisotropy and the overall ground state of the molecule in transition metal complexes,[11] while the QTM is responsible for the faster relaxation in lanthanide complexes.[1f,12] The qualitative prediction about the influence of

electronic structures and suitable ligand field around lanthanide complexes was very well exemplified by Long and co-workers in 2011.[7] Using this elegant approach, in fact, several mononuclear dysprosium(III) and erbium(III) complexes were reported to stabilize the record-breaking magnetization reversal barrier (U_{eff}) with significantly improved blocking temperatures (10−60 K), and this has been firmly supported by computational calculations.[10b−f,13] Compared to the naked dysprosium(III) complexes, low-coordinated dysprosium(III) encapsulation in fullerene cages was observed to be a promising approach, which facilitates enhancement of the blocking temperature.[14] To the extent that the SMM or SIM behavior was investigated for dysprosium(III) complexes, slow magnetization of relaxation for the other lanthanide ions is scarcely studied in the literature.[1g,13,15]

In this line of interest, we have isolated a series of lanthanide monomeric complexes using a Schiff base ligand, 2-methoxy-6-[(E)-phenyliminomethyl]phenol (HL). The influence and suitability of the ligand field around the Er^{III} ion using HL was reported earlier by us elsewhere.[15a] In a natural extension of this study, we have now isolated three more paramagnetic complexes along with their diamagnetic analogues, which are reported in this article. The isolated new complexes are structurally analogous to the earlier-reported erbium(III) and dysprosium(III) complexes[15a,16] confirmed by single-crystal X-ray diffraction (XRD). A structural investigation of the new complexes reveals the molecular formulas to be [Ce(HL)$_3$(NO$_3$)$_3$] (1) and [Ln(HL)$_2$(NO$_3$)$_3$], where Ln^{III} = Tb (2), Ho (3), Er (4), and Lu (5). For complexes 1−4, detailed direct (dc) and alternating-current (ac) magnetic susceptibility studies were performed on the polycrystalline sample. The experimental observations are rationalized by theoretical calculations, which further give more insight into the mechanism of magnetization relaxation (vide infra).

MATERIALS AND METHODS

All of the reactions were carried out under aerobic conditions. All of the chemicals and solvents were purchased from commercially available sources (Alfa aeser) and used without further purification. Ligand HL was synthesized as per the literature report.[17] IR spectra were recorded for the solid samples using KBr pellets on a Perkin-Elmer Fourier transform infrared (FT-IR) spectrometer in the 400−4000 cm^{-1} range. Elemental analyses (C, H, and N) were carried out on a Thermoquest microanalyzer. Powder XRD data were collected using a Panalytical EMPYREAN model X-ray powder diffractometer. Magnetic susceptibility measurements were performed on polycrystalline sample of complexes 1−4 using an MPMS SQUID magnetometer equipped with a 7 T magnet in the 300−1.8 K temperature range. Ac magnetic susceptibility measurement below 1.8 K for 4 was performed using an I-Helium3 setup (Quantum Design, USA). Single-crystal data were collected on a Rigaku Saturn diffractometer (Mo Kα, λ = 0.71073 Å). Suitable crystals were mounted on a fiber loop using Paratone-N oil and positioned in the cold flow produced with an Oxford cryocooling device. Complete hemispheres of data were collected by using ω and φ scans (0.3 Å and 30 s/frame). Integrated intensities were gained with *SAINT+/CrystalClear-SM Expert* (Rigaku 2012), and they were corrected for absorption using *SADABS*. Structure solution and refinement were performed with the *SHELX-2014* package. The structures were solved by direct methods and completed by iterative cycles of ΔF syntheses and full-matrix least-squares refinement against F^2.

COMPUTATIONAL DETAILS

Ab Initio Calculations. Ab initio calculations were performed on the Ln^{III} ions in complexes 1−4 using the *MOLCAS 8.0* suite of

software.[18] Relativistic effects are taken into account on the basis of the Douglas−Kroll Hamiltonian.[19] The spin-free eigenstates were achieved by the complete active space self-consistent-field (CASSCF) method.[20] We employed the ANO-RCC···8s7p5d3f2g1h basis set[21] for Ce, Tb, Ho, and Er atoms, the ANO-RCC···3s2p basis set for C atoms, the ANO-RCC···2s basis set for H atoms, the ANO-RCC···3s2p1d basis set for N atoms, and the ANO-RCC···3s2p1d basis set for O atoms. CASSCF calculations were performed and included 1 electron in seven 4f orbitals of the Ce^{III} ion (1,7), 8 electrons in seven 4f orbitals of the Tb^{III} ion (8,7), 10 electrons in seven 4f orbitals of the Ho^{III} ion (10,7), and 11 electrons in seven 4f orbitals of the Er^{III} ion (11,7) in 1−4 respectively. With this active space, 7 roots for doublet were computed for complex 1. We have considered 7 septet excited states, 86 quintet excited states, and 60 triplet excited states for complex 2 and 35 quintet excited states, 106 triplet excited states for complex 3 in the calculations to compute the anisotropy. For complex 4, 35 quartets and 112 doublets using the configuration interaction procedure were considered to compute the anisotropy. After computing all of these excited states, we have mixed all of these states for the individual complexes using the RASSI-SO module to compute the spin−orbit coupled states.[22] Moreover, these computed spin−orbit states have been considered into the *SINGLE_ANISO* program to compute the **g** tensors of complexes 1−4.[23] The Cholesky decomposition for two-electron integrals is employed throughout in calculations to reduce the disk space. Crystal-field parameters were extracted using the *SINGLE_ANISO* code, as implemented in *MOLCAS 8.0*.[18]

EXPERIMENTAL METHODS

Synthesis of the Complex [Ce(NO$_3$)$_3$(HL)$_3$] (1). To an ethanolic solution of HL (0.3 g, 1.32 mmol) was added Ce(NO$_3$)$_3$·6H$_2$O (0.2869g, 0.62 mmol) at room temperature, and the reaction mixture was heated under reflux for 7−8 h. After that, the reaction mixture was concentrated and filtered. This resultant filtrate was allowed to stand at 3−7 °C without any disturbance. Single crystals of complex 1 suitable for XRD were obtained after 3 days. FT-IR (KBr pellets, cm^{-1}): 3428 (m, ν_{N-H}), 2972 (s, ν_{Ar-H}), 1638 (s, $\nu_{C=N}$). Elemental anal. Calcd: C, 50.05; H, 3.90; N, 8.34. Found: C, 49.96; H, 3.75; N, 8.30. Yield (based on Ce^{3+}): 0.24 g (35.9%).

Synthesis of Complexes [Ln(NO$_3$)$_3$(HL)$_2$] [Where Ln = Tb (2), Ho (3), Er (4), and Lu (5)]. A synthetic procedure similar to that of 1 was followed for the isolation of complexes 2−5, but Ce(NO$_3$)$_3$·6H$_2$O was replaced with the corresponding lanthanide precursors Tb(NO$_3$)$_3$·xH$_2$O (0.2279 g, 0.62 mmol), Ho(NO$_3$)$_3$·5H$_2$O (0.2215 g, 0.62 mmol), Er(NO$_3$)$_3$·5H$_2$O (0.2926 g, 0.62 mmol), and Lu(NO$_3$)$_3$·xH$_2$O (0.2385 g, 0.62 mmol). In all cases, single crystals were obtained from the filtrate upon crystallization at 3−7 °C similar to 1; however, the crystals were not of good quality to characterize by single-crystal XRD. Hence, after completion of the reaction, ethanol was removed from the reaction mixture under reduced pressure, and the resultant crude mixture was recrystallized from methanol. Single crystals of complexes 2−5 were grown from the filtrate within 2−3 days while standing at 3−7 °C undisturbed which are suitable for X-ray diffraction.

For 2. FT-IR (KBr pellets, cm^{-1}): 3437 (m, ν_{N-H}), 2920 (s, ν_{Ar-H}), 1636 (s, $\nu_{C=N}$). Elemental anal. Calcd: C, 42.06; H, 3.27; N, 8.76. Found: C, 42.23; H, 3.43; N, 8.76. Yield (based on Tb^{3+}): 0.18 g (34.4%).

For 3. FT-IR (KBr pellets, cm^{-1}): 3431 (m, ν_{N-H}), 2963 (s, ν_{Ar-H}), 1638 (s, $\nu_{C=N}$). Elemental anal. Calcd: C, 41.75; H, 3.25; N, 8.69. Found: C, 42.26; H, 3.50; N, 8.75. Yield (based on Ho^{3+}): 0.27 g (51.17%).

For 4. FT-IR (KBr pellets, cm^{-1}): 3423 (b, ν_{N-H}), 2930.17 (s, ν_{Ar-H}), 1642.24 (s, $\nu_{C=N}$). Elemental anal. Calcd: C, 41.63; H, 3.24; N, 8.67. Found: C, 41.60; H, 3.22; N, 8.59. Yield (based on Er^{3+}): 0.29 g (54.89%).

For 5. FT-IR (KBr pellets, cm^{-1}): 3412 (m, ν_{N-H}), 2933 (s, ν_{Ar-H}), 1636 (s, $\nu_{C=N}$). Elemental anal. Calcd: C, 41.23; H, 3.21; N, 8.58. Found: C, 41.26; H, 3.19; N, 8.55. Yield (based on Lu^{3+}): 0.20 g (37.86%).

Synthesis of a 50% Dilution Sample of 4. A magnetically diluted (50%) sample was prepared by reacting the ligand HL (0.3 g, 1.3 mmol) with $Lu(NO)_3 \cdot xH_2O$ (0.1192 g, 0.33 mmol) and $Er(NO_3)_3 \cdot 5H_2O$ (0.1464 g, 0.33 nmol) in ethanol. The resulting mixture was refluxed for 7−8 h. The solvent was removed under reduced pressure. The obtained crude mixture was recrystallized from methanol. The isolated polycrystalline material was used for magnetic measurements.

Note that the phase purities of all of the complexes were confirmed by the powder XRD method. The experimental powder XRD pattern is in excellent agreement with the simulated data generated from the single-crystal XRD pattern of their respective complexes (Figures S1−S4).

■ RESULTS AND DISCUSSION

The reaction between 2 equiv of the ligand HL and 1 equiv of lanthanide(III) nitrate salt (where Ln = Ce[III], Tb[III], Ho[III], Er[III], and Lu[III]) in ethanol followed by crystallization in methanol/ethanol resulted in the formation of orange-red single crystals. XRD analysis revealed the identity of the complexes with the molecular formula for Ce(III) ion as $[Ce(HL)_3(NO_3)_3]$ (**1**) and those for other Ln ions with the general formula $[Ln(HL)_2(NO_3)_3]$ [where Ln = Tb[III] (**2**), Ho[III] (**3**), Er[III] (**4**), and Lu[III] (**5**)]. The general synthetic procedure followed for the isolation of complexes **1**−**5** is shown in Scheme 1.

Scheme 1. Schematic Presentation for the Synthetic Route for Complexes 1−5
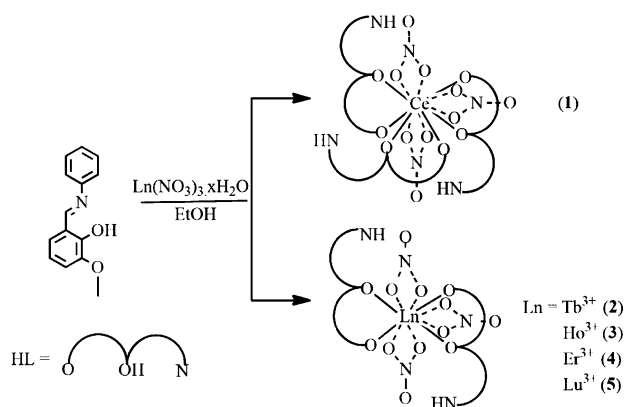

Structural Description of Complexes 1−5. Complex **1** crystallized in the triclinic $P\bar{1}$ space group, and its crystal structure is shown in Figure 1. Crystallographic parameters for **1** are given in Table 1. The Ce(III) ion in **1** is surrounded by 12 O-donor atoms. A total of 6 out of 12 coordination sites were derived from three chelating bidenate nitrate ions, while the remaining 6 coordination sites are completed by the phenoxy and methoxy O atoms of three HL ligands. The average Ce−O(phenoxo), Ce−O(methaoxo), and Ce−O(nitrate) bond lengths were found to be 2.449(4), 3.019(4), and 2.646(5) Å, respectively.

The 12-coordinated Ce(III) ion exhibits distorted icosahedron geometry, which was confirmed by Continuous-Shape Measurement (CShM) software (Table S1).[24] In **1**, the entire molecule behaves as an asymmetric unit (ASU). Selected bond lengths are given in Table 2.

Detailed analysis of the packing diagram of **1** revealed that the nitrate ions coordinated to the Ce(III) ion in **1** facilitate intermolecular hydrogen bonding (Figure 2 and Table S2). The closest Ce···Ce distance was found to be 9.924 Å.

On the other hand, unlike **1**, complexes **2**−**5** crystallized in the Aba2 space group with an orthorhombic crystal system (Table 1). Single-crystal XRD revealed that complexes **2**−**5** are also monomers, but these structures differ from **1** by the number of HL ligands coordinated to the metal center. In **1**, there are three neutral HL ligands, while in the case of **2**−**5**, only two neutral HL ligands were found to be coordinated to the Ln(III) ions. Hence, for all of the lanthanide complexes (**2**−**5**), the coordination number is 10. The relatively low coordination numbers in **2**−**5** compared to that in **1** are likely due to lanthanide contraction,[25] which is also responsible for the comparatively short bond lengths observed for Ln−O (phenoxo, alkaloxo, and nitrate) in **2**−**5** than in **1** (see Table 2).

All four complexes (**2**−**5**) were structurally analogous to each other, which is evident from the similar unit cell parameters observed for all of these complexes (Table 1). Hence, a representative structure (complex **4**) for this series is shown in Figure 3 (also see Figure S5) and its structural description is detailed below. Apart from the change in the coordination number of **2** compared to **1**, the ASUs of **2**−**5** are distinctly different from that of **1**; i.e., the ASU of **2** contains one crystallographically distinct complete molecule (labeled as **2a**)
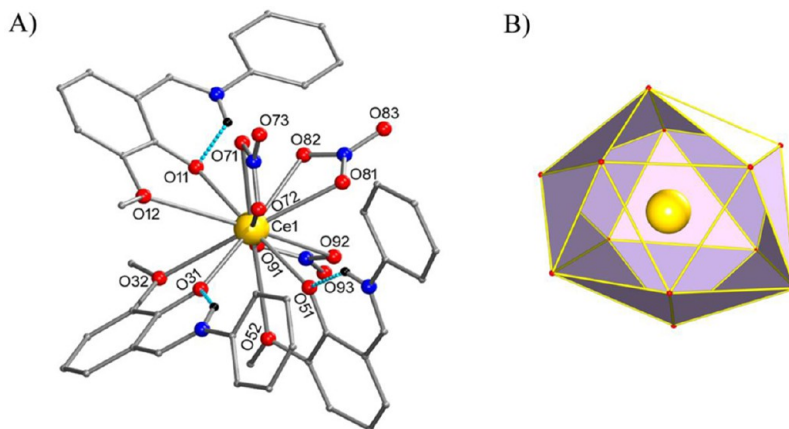
Figure 1. (A) Ball and stick representation for the crystal structure of **1**. Blue dotted bonds denote intramolecular hydrogen bonding. (B) Polyhedral view showing icosahedron geometry around the Ce(III) ion in **1**. Color code: yellow, Ce(III); blue, N; red, O; gray, C.

Table 1. Crystallographic Parameters for Complexes 1−5

	1	2	3	4	5
formula	$Ce_1C_{42}H_{39}N_6O_{15}$	$Tb_1C_{28}H_{26}N_5O_{13}$	$Ho_1C_{28}H_{26}N_5O_{13}$	$Er_1C_{28}H_{26}N_5O_{13}$	$Lu_1C_{28}H_{26}N_5O_{13}$
size	0.33 × 0.16 × 0.05	0.15 × 0.41× 0.10	0.29 × 0.06 × 0.05	0.2 × 0.19 × 0.15	0.21 × 0.15 × 0.17
system	triclinic	orthorhombic	orthorhombic	orthorhombic	orthorhombic
space group	$P\bar{1}$	$Aba2$	$Aba2$	$Aba2$	$Aba2$
a [Å]	11.180(2)	17.709	17.620(4)	17.572(5)	17.439(3)
b [Å]	11.831(2)	54.28	54.041(12)	54.043(16)	54.451(11)
c [Å]	16.392(3)	9.639	9.591	9.580(3)	9.5702(19)
α [deg]	81.763(7)	90	90	90	90
β [deg]	79.264(6)	90	90	90	90
γ [deg]	79.488(7)	90	90	90	90
V [Å^3]	2081.0(6)	9265(6)	9133(3)	9098(5)	9088(3)
Z	2	4	12	12	12
ρ_{calcd}[g cm^{-3}]	1.609	1.719	1.757	1.769	1.788
$2\Theta_{max}$	58.20	50	58.38	58.30	58.24
radiation	Mo Kα	Mo Kα	Mo Kα	Mo Kα	Mo Kα
λ [Å]	0.71070	0.71070	0.71070	0.71075	0.71075
T [K]	100	100	100	100	100
no. of reflns	27025	27052	55974	59128	55796
no. of indep reflns	11121	7227	12314	11965	12162
no. of reflns with >2$\sigma(I)$	8909	5934	11023	10593	10958
R1	0.0331	0.0371	0.0613	0.0830	0.0446
wR2	0.0587	0.0947	0.1343	0.1964	0.0807

Table 2. Selected Bond Lengths for Complexes 1−5

|			1			
Ce1−O12	2.434(14)	Ce1−O32	3.068(5)	Ce1−O72		2.634(15)
Ce1−O51	2.447(13)	Ce1−O52	3.010(4)	Ce1−O91		2.635(15)
Ce1−O31	2.466(13)	Ce1−O71	2.652(16)	Ce1−O81		2.712(14)
Ce1−O82	2.580(15)	Ce1−O92	2.667(15)	Ce1−O11		2.877(16)
	2a	**3a**	**4a**		**5a**	
M1−O11	2.274(4)	2.298(5)	2.247(6)	Lu1−O11		2.229(3)
M1−O12	2.701(4)	2.740(5)	2.685(5)	Lu1−O12		2.975(4)
M1−O31	2.312(4)	2.263(5)	2.262(6)	Lu1−O31		2.231(3)
M1−O32	2.737(4)	2.700(5)	2.803(5)	Lu1−O32		2.647(3)
M1−O71	2.528(9)	2.437(6)	2.527(5)	Lu1−O71		2.509(9)
M1−O72	2.470(10)	2.434(6)	2.486(6)	Lu1−O72		2.430(4)
M1−O51	2.470(5)	2.412(12)	2.543(7)	Lu1−O51		2.418(3)
M1−O52	2.478(5)	2.5020(9)	2.478(5)	Lu1−O52		2.412(10)
M1−O61	2.471(7)	2.442(8)	2.415(6)	Lu1−O61		2.334(8)
M1−O62	2.507(4)	2.502(6)	2.388(6)	Lu1−O62		2.393(9)
	2b	**3b**	**4b**		**5b**	
M2−O111	2.288(5)	2.266(5)	2.234(5)	Lu2−O111		2.219(3)
M2−O112	2.574(5)	2.537(5)	2.543(6)	Lu2−O112		2.529(4)
M2−O151	2.472(4)	2.875(9)	2.511(4)	Lu2−O151		2.437(4)
M2−O152	2.540(4)	2.446(5)	2.432(5)	Lu2−O171		2.386(4)
M2−O161	2.505(5)	2.494(5)	2.634(6)	Lu2−O161		2.532(4)

and another half-molecule (labeled as **2b**, total of one and a half molecule) present in the unit cell. The entire molecule of **2b** is generated by rotational and/or inversion symmetry. A similar scenario is observed in all other structurally analogous complexes as well (**3**−**5**); the crystallographically distinct molecules in the unit cell are labeled as **3a** and **3b** (for **3**), **4a** and **4b** (for **4**), and **5a** and **5b** (for **5**). Although molecules *n***a** and *n***b** (*n* = 2, 3, 4, or 5) contain the same molecular formula, i.e., three chelating nitrate ions and two neutral HL ligands, the orientations of the nitrates and Schiff base ligands are distinctly different from one another. In *n***a** (*n* = 2, 3, or 4, or 5), the three chelating nitrate ions are arranged in a near-trigonal-planar

arrangement (see Figure 3A) around the central Ln(III) ion and the two Schiff base ligands are chelated to the metal ion and lie above and below the trigonal-planar arrangement of the nitrates.

The average ∠N−Ln−N angles in the cases of *n***a** (*n* = 2, 3, 4, or 5) were found to be 119.92°, 119.95°, 120°, and 119.48° for **2**−**5**, respectively. In the case of *n***b** (*n* = 2, 3, 4, or 5) molecules, the nitrate ion orientation is distinctly different from that of *n***a** molecules; this is clearly reflected from its average ∠N−Ln−N angles of 73.51°, 73.16°, 73.63°, and 73.69° for **2**−**5**, respectively. The different orientations of the nitrates in *n***a** and *n***b** likely influence the electronic structures of these
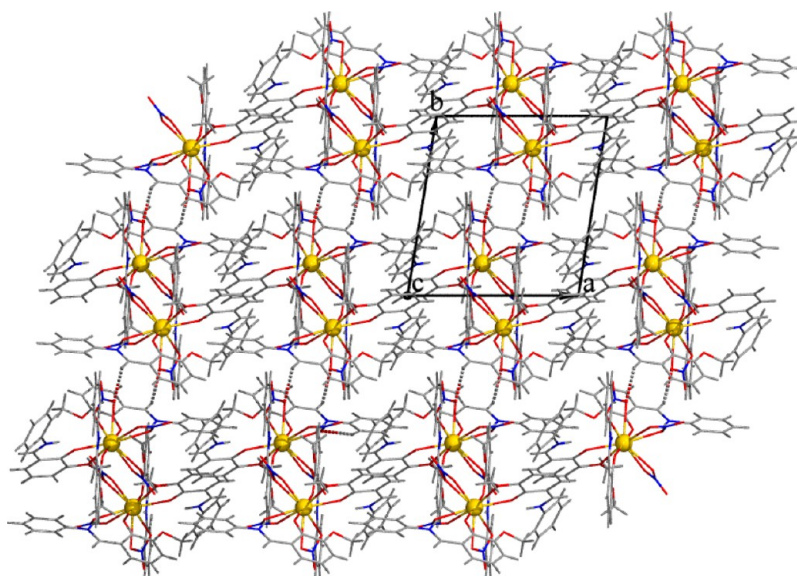
Figure 2. Packing diagram of complex **1** (view along the *c* axis). Dotted bonds connecting two molecules represent intermolecular hydrogen bonding.
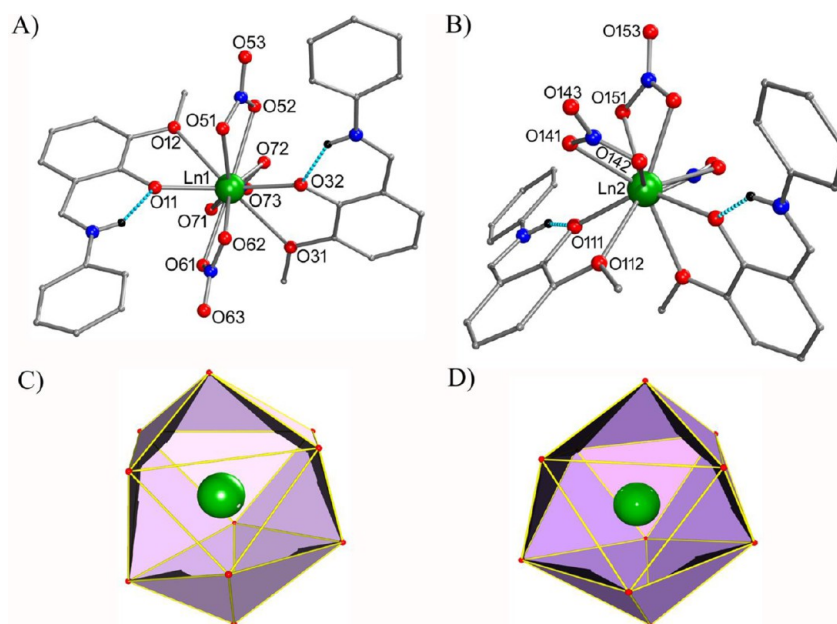
Figure 3. (A) Ball-and-stick representations for the crystal structures of (A) **4a** and (B) **4b**. Color code: green, Er(III); blue, N; red, O; gray, C. The dotted sky-blue bond denotes intramolecular hydrogen bonding. Panels C and D represent the sphenocorona and bicapped square-antiprismatic geometries observed around the **4a** and **4b** molecules in the crystal lattice of **4**, respectively.

molecules, and the effect will vary depending on the prolate or oblate electron density around the Ln(III) ions in **2**−**5** (vide infra). To the best of our knowledge, such structural isomers crystallizing in the same unit cell are relatively rare in the literature and are reported by us for the first time, although the coordination isomers are known.[16b,26] In addition to the above-observed difference, the geometry around the crystallo-graphically distinct molecules *na* and *nb* (where *n* = 2, 3, 4, or 5) in the crystal lattice of the each complex varies significantly, confirmed by *CShM* software (Table S3).[24] The geometry around one of the geometrical isomers, *nb* (where *n* = 2−5), was found to be a distorted bicapped square-antiprismatic geometry (~D_{4d}). The extent of distortion observed in the geometry of *nb* molecules decreases as the

ionic radii decrease (Table S3). In contrast, the *CShM* value of the *na* (where *n* = 2−5) molecule suggests that this particular isomer possesses a distorted sphenocorona geometry (~C_{2v}). The *CShM* values of *na* and *nb* (where *n* = 2−5) molecules evidently show that *nb* (where *n* = 2−5) molecules possess higher symmetry than *na* (where *n* = 2−5) molecules in the crystal lattices of **2**−**5**. Analyses of the packing diagram of these complexes again revealed that the closest Ln···Ln distances found were 9.263, 10.031, 9.264, and 9.946 Å for **2**−**5**, respectively (Figure 4). In all five complexes (**1**−**5**), the trivalent cationic charge on the metal ion is compensated by the three nitrate ions coordinated to it. Detailed structural analysis of all of the complexes (**1**−**5**) reveals that the proton bound to the phenoxy O atom of a metal-free Schiff base ligand migrates
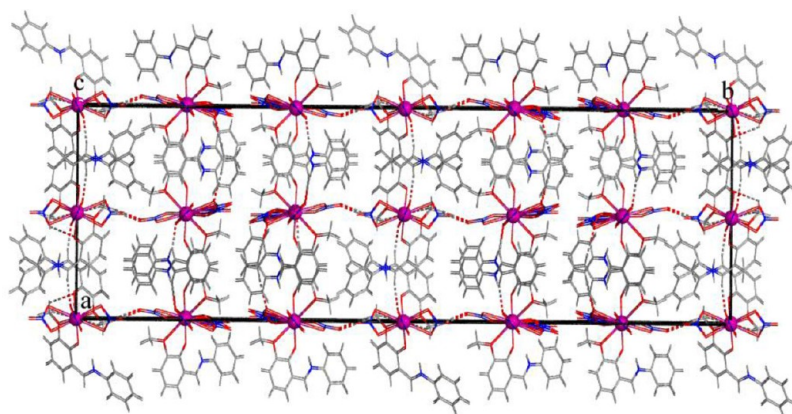
Figure 4. Packing diagram of **2** as a representative packing diagram for the structurally analogous complexes **2**–**5**. Dotted lines represent intermolecular hydrogen bonding.

to the N atom of the imino group upon coordination to the metal ions in **1**–**5**.

Migration of the H atom of the phenoxy group to the imine N atom (−C=N) was confirmed by the decreased bond length of C−O (1.305−1.324 Å) in all of the complexes compared to the free ligand (1.350 Å). Thus, in all of the complexes, the Schiff base ligand exists in a zwitterionic form. The existence of a zwitterionic form of this ligand is confirmed by NMR studies in a diamagnetic analogue of complex **1** ([La(HL)$_3$(NO$_3$)$_3$]), which was reported elsewhere by us and others.[17b,27] Because of protonation, this iminium group does not participate in metal coordination; however, this proton was found to be involved in intramolecular hydrogen bonding with the quinone O atom of the ligand. Apart from intramolecular hydrogen bonding, the atoms involved in intermolecular hydrogen bonding in all of the complexes are listed in Table S2.

dc Magnetic Susceptibility Measurement. Temperature-dependent dc magnetic susceptibility measurements were performed on polycrystalline samples of complexes **1**–**4** at 2−300 K with an external magnetic field of 1 kOe (Figure 5A).

Detailed electronic and magnetic properties of isotropic gadolinium(III) and dysprosium(III) complexes were reported by us elsewhere.[16,28] The temperature-dependent magnetic behaviors of complexes **2**–**4** were found to show very similar trends. The room temperature $\chi_M T$ value for complexes **1**–**4** was found to be 0.83, 11.91, 13.83, and 11.48 cm^3 K mol^{-1}, respectively. These observed values at room temperature are in close agreement with the expected value (Table 3).

Upon cooling from room temperature, the $\chi_M T$ values for all of the complexes **2**–**4** gradually decrease before they precipitously drop below 50 K (for **2**) and 100 K (for **3** and **4**). The gradual decrease in $\chi_M T$ [from room temperature to 50 K (for **2**) or 100 K (for **3** and **4**)] may be ascribed to thermal depopulation of the m_j levels of Ln(III) ions while a sudden decrease at low temperature (below 50 K) is likely due to the anisotropy and/or intermolecular antiferromagnetic interactions and/or dipolar interactions. In contrast to complexes **2**–**4**, complex **1** shows strong temperature-dependent magnetic susceptibility from room temperature to low temperature. Several parameters such as thermal depopulation of the Stark levels, anisotropy, intermolecular antiferromagnetic interaction, and/or dipolar interaction are likely to contribute for this observed temperature-dependent behavior in **1**.
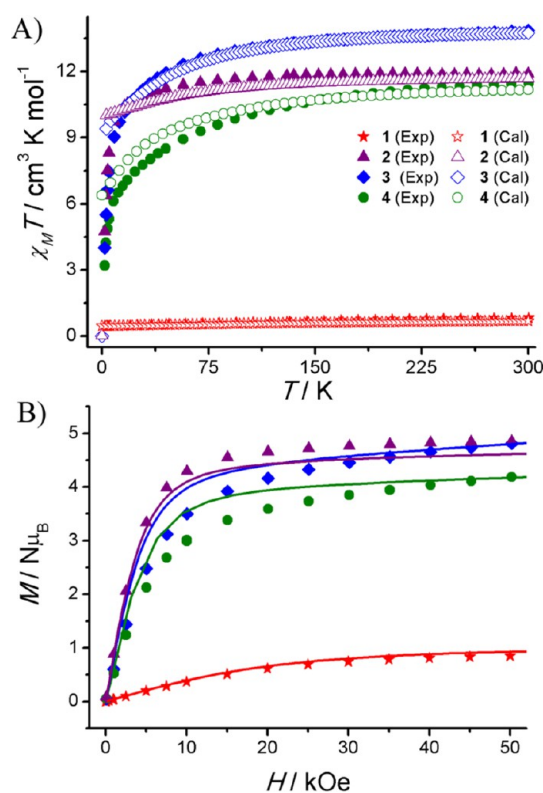
Figure 5. (A) Temperature-dependent dc magnetic susceptibility and temperature product of complexes **1**–**4** measured at 1 kOe (filled symbol). (B) Field-dependent magnetization measurement performed on polycrystalline samples of **1**–**4** at 2.0 K. Open symbol/solid lines represent the computed $\chi_M T$ and M values for the indicated complexes.

Table 3. Experimental $\chi_M T$ Values of 1−4 and Their Expected $\chi_M T$ Values along with Their Crystal-Field Term Symbols

complex	$\chi_M T$ (cm^3 K mol^{-1})		crystal-field term	g	S	L	J
	exptl	calcd					
1	0.83	0.80	$^2F_{5/2}$	$^6/_7$	$^1/_2$	3	$^5/_2$
2	11.91	11.81	$^7F_6$	$^3/_2$	3	3	6
3	13.83	14.06	$^5I_8$	$^5/_4$	2	6	8
4	11.48	11.07	$^4I_{15/2}$	$^6/_5$	$^3/_2$	6	$^{15}/_2$
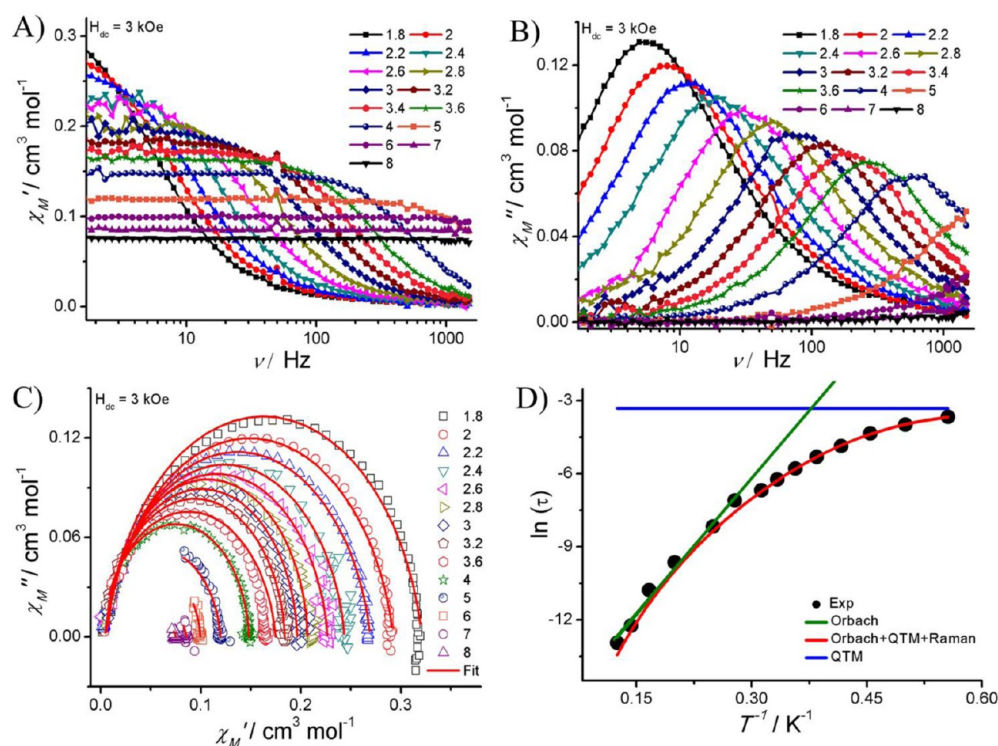
Figure 6. Field-induced frequency-dependent in-phase (panel A) and out-of-phase (panel B) susceptibility measurements performed on a polycrystalline sample of **1** at the indicated temperature. (C and D) Cole−Cole and Arrhenius plots of complex **1**, respectively. The solid red traces in both panels C and D represent the best fits obtained for the experimental data using the parameters described in the main text.

Isothermal magnetization for complexes **1**−**4** was recorded between 2 and 8 K in the presence of an external magnetic field (Figures 5B and S6) up to 50 kOe. Upon an increase of the magnetic field at 2.0 K for all of the complexes (**1**−**4**), a steep increase in the magnetic moment was initially observed. This is due to the Zeeman interaction induced population of the ground-state m_j levels in all of the complexes. For **1**, a further increase in the external magnetic field has little influence on the magnetic moment (0.85 Nμ_B at 50 kOe) value, while for complexes **2**−**4**, the magnetic moments tend to saturate around 4.85, 4.80, and 3.80 Nμ_B, respectively. The obtained M_{sat} values were lower than the theoretical values (2.1, 9, 10, and 9 Nμ_B for complexes **1**−**4**, respectively). This implies the presence of anisotropy associated with all of the complexes, which is strongly corroborated by the non-superimposable nature of reduced magnetization curves of complexes **1**−**4** (Figure S7).

Ac Magnetic Susceptibility Measurement. To probe the relaxation dynamics, ac susceptibility measurements were performed on polycrystalline samples of **1**−**4** with an oscillating magnetic field of 3.5 Oe between the temperature ranges of 1.8−8 K for complexes **1**−**3** and 0.5−8 K for **4** in the presence and absence of an optimum external magnetic field. For complexes **1**−**3**, frequency-dependent out-of-phase susceptibility signals were not observed in the absence of an external magnetic field (data not shown). The absence of χ_M'' signals in **1**−**3** indicates that QTM is dominant compared to a thermally activated relaxation mechanism such as the Orbach process. This kind of behavior is well-known for many low-symmetric lanthanide-based complexes.[1b,f,8q,29] Often QTM can be suppressed or quenched to some extent by the application of an external magnetic field. To find out the optimum external magnetic field, field-sweep measurements were performed for complexes **1**−**3** (Figures S8−S10). Detailed ac measurement

for complex **1** was performed in the presence of an optimum external magnetic field of 3 kOe (Figure 6). In the presence of a bias field, frequency-dependent out-of-phase susceptibility signals show well-resolved peaks with a clear maximum at the indicated temperature. The presence of a single peak in χ_M'' susceptibility unambiguously confirms that the magnetization vector predominantly follows the thermally activated relaxation pathway (Orbach process).

The presence of a predominant single relaxation pathway is further confirmed by a Cole−Cole plot. The Cole−Cole plot was fitted using the generalized Debye eq 1 (where χ_S, χ_T, ω, and α are the adiabatic susceptibility, isothermal susceptibility, angular frequency of ac, and Cole−Cole parameters, respectively), considering a single relaxation process. Excellent fits were obtained for the parameters listed in Table S4, with α values ranging from 0.03 to 0.29 indicating the distribution of the single relaxation process, which might arise because of intermolecular and/or dipolar interactions between the molecules.

$$\chi_{ac}(\omega) = \chi_S + \frac{\chi_T - \chi_S}{1 + (i\omega\tau)^{1-\alpha}} \tag{1}$$

An Arrhenius plot was constructed using the τ values obtained by the Cole−Cole fitting shown in Figure 6D. The Arrhenius plot tends to deviate from linearity at low temperature (<2.5 K); this indicates that, in addition to the thermally assisted Orbach relaxation process, QTM and other alternative relaxation processes appear to be operative even in the presence of an optimum external magnetic field. The Arrhenius plot of **1** over the entire temperature range was fitted by multiple relaxation pathways using eq 2.
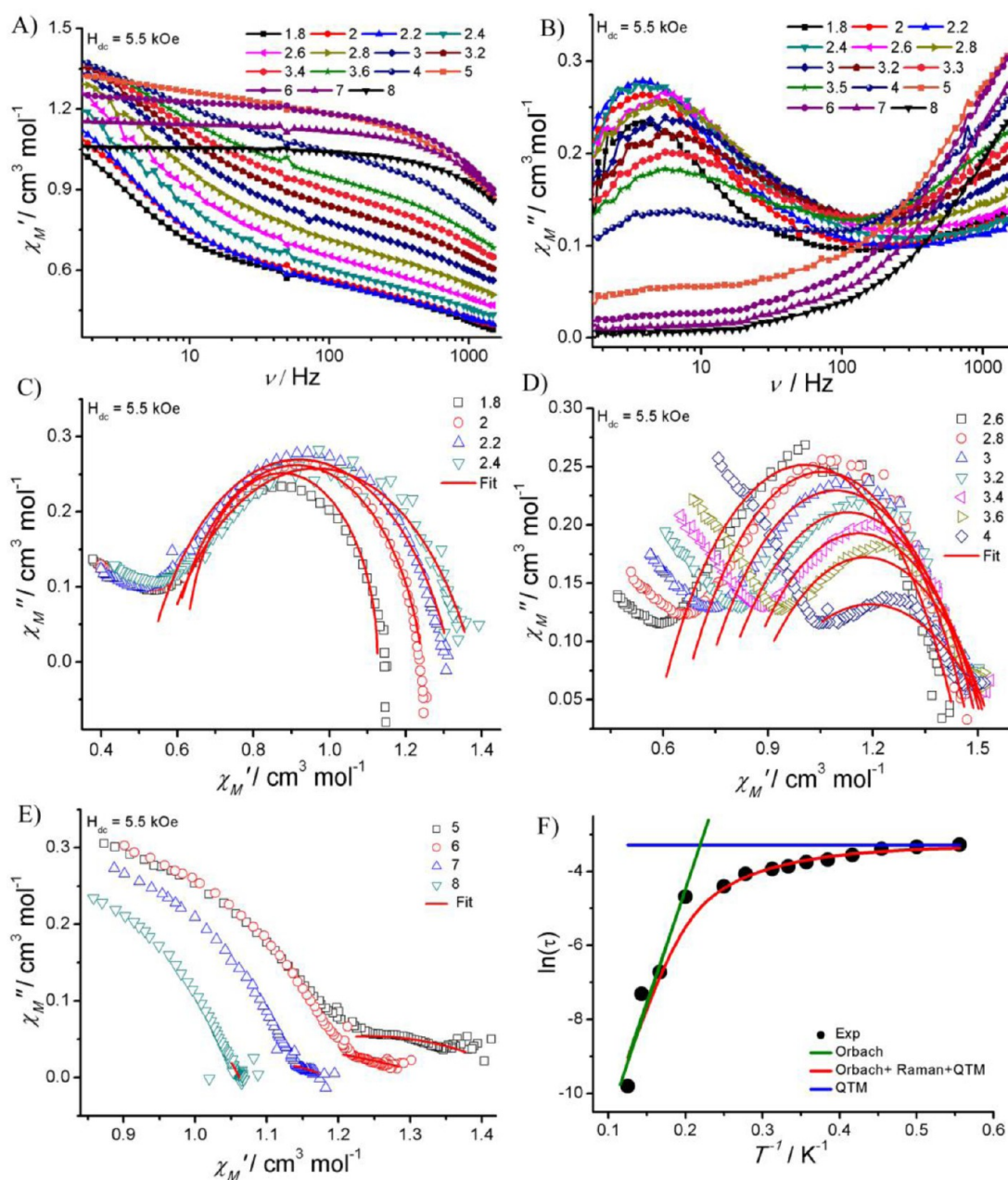
Figure 7. Field-induced frequency-dependent in-phase (panel A) and out-of-phase (panel B) susceptibility measurements performed on a polycrystalline sample of **2** at the indicated temperature. (C−E) Cole−Cole plots of complex **2** at the indicated temperature ranges. (F) Arrhenius plot of **2** constructed using the Cole−Cole fitting parameters (τ) of **2**. The solid red traces in panels C−F represent the best fits obtained for the experimental data using the parameters described in the main text.

$$\frac{1}{\tau} = \frac{1}{\tau_{QTM}} + CT^n + \tau_0^{-1}\exp\left(\frac{-U_{eff}}{k_BT}\right) \qquad (2)$$

The first term on the right-hand side of eq 2 represents the reversal of magnetization through QTM, the second term denotes relaxation via the Raman process, and the final term corresponds to the thermally assisted (Orbach) relaxation mechanism. The best fit to the data was obtained by considering the Orbach (U_{eff} = 26.06 cm^{-1} and τ_0 = 2.76 × 10^{-8} s), Raman (C = 0.154 s^{-1} K^{-n} and n = 7.36), and QTM (τ_{QTM} = 0.076 s) processes [Figure 6D (red trace)] in the presence of a 3 kOe applied field. Only a limited number of cerium(III) complexes are reported in the literature, of which the observation of slow relaxation of magnetization is even

more slim.[30] Considering this aspect, the observation of slow magnetization of relaxation in **1** makes this complex a valuable addition. The observed energy barrier is comparable with those of earlier literature reports.[30b−e]

For **2**, the optimum external magnetic field was found to be 5.5 kOe (Figure S9). Even at this external magnetic field, multiple relaxation pathways are present; however, the thermally activated relaxation behavior is dominant over that of the other faster relaxation process. Hence, detailed frequency sweep ac susceptibility measurements between 1.8 and 8 K were performed in the presence of an external magnetic field of 5.5 kOe (Figure 7). From Figure 7, it is evident that there is more than one relaxation process, which was further supported by the Cole−Cole plot. The observation of more than one
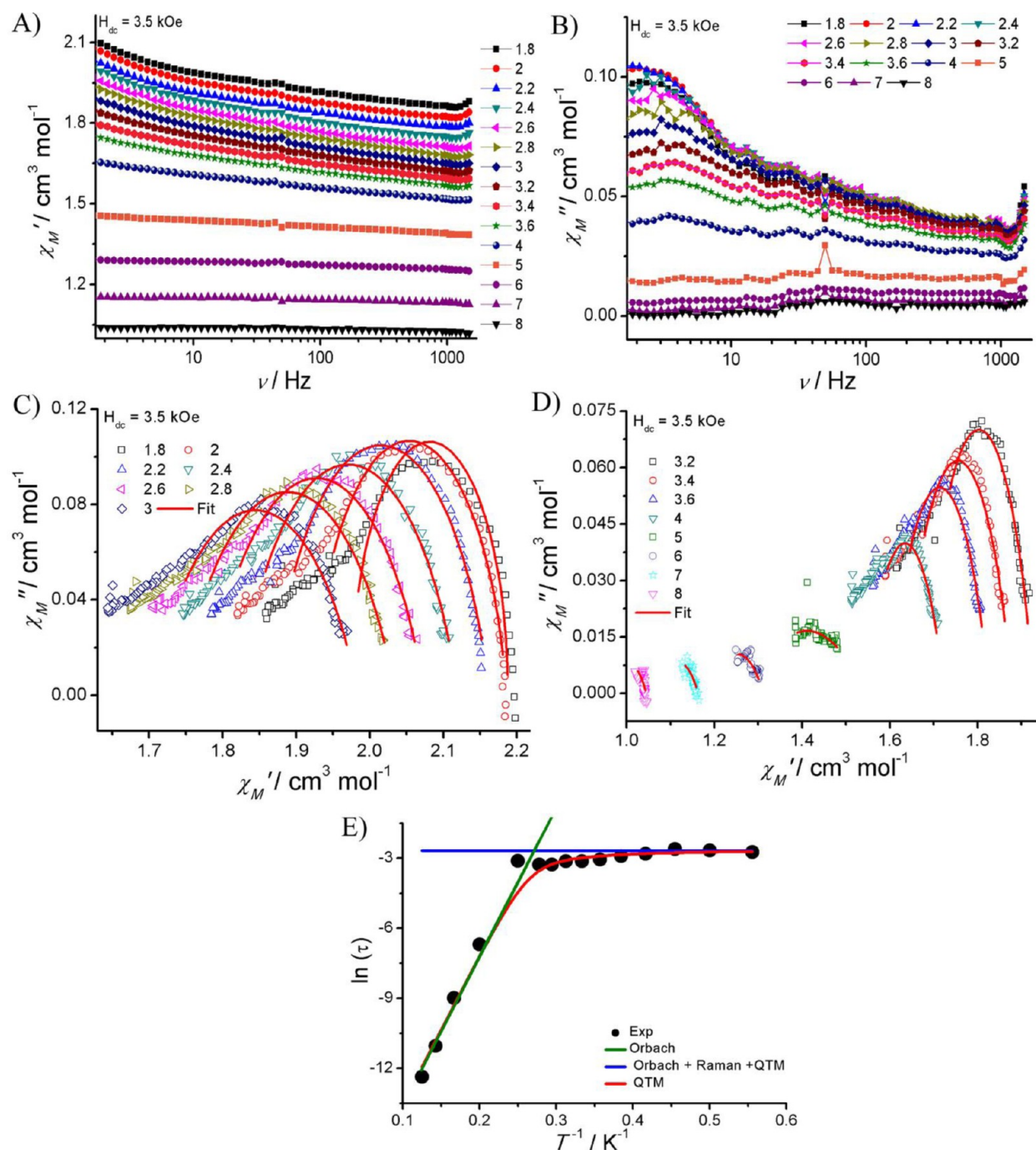
Figure 8. Field-induced frequency-dependent in-phase (panel A) and out-of-phase (panel B) susceptibility measurements performed on a polycrystalline sample of **3** at the indicated temperature. (C and D) Cole−Cole plots of complex **3** at the indicated temperature range. (E) Arrhenius plot of **3** constructed using the Cole−Cole fitting parameters (τ) of **3**. The solid red traces in panels C and D represent the best fits obtained for the experimental data using the parameters described in the main text.

relaxation process for mononuclear lanthanide complexes was witnessed in the literature earlier.[30b,31] For example, [Dy^{III}DOTA] complexes were found to show Raman and QTM in addition to the Orbach relaxation process reported by Sessoli and co-workers.[32] The presence of multiple relaxations in **2** is likely due to several factors: (1) since **2a** and **2b** possess different geometries, more than one relaxation may arise; (2) due to significant distortion in the geometry, the transverse component of g anisotropy may open up QTM; (3) dipolar interaction between the molecules. In order to determine the origin of multiple relaxation processes in **2**, it is important to

isolate one of the structural isomers (either **2a** or **2b**) separately. However, attempts were failed to isolate these isomers using HL in different conditions. The Cole−Cole plot was fitted considering only the major relaxation process. The data were fitted using eq 1. The fitted plots are shown in Figures 7C−E, and their corresponding fitting parameters are shown in Table S5. The relaxation time extracted from the Cole−Cole data fitting was used for construction of the Arrhenius plot. The effective energy barrier (U_{eff}) for magnetization reversal for complex **2** was extracted using eq 2, which was found to be 42 cm^{-1}, $\tau_0 = 6.31 \times 10^{-8}$ s, Raman
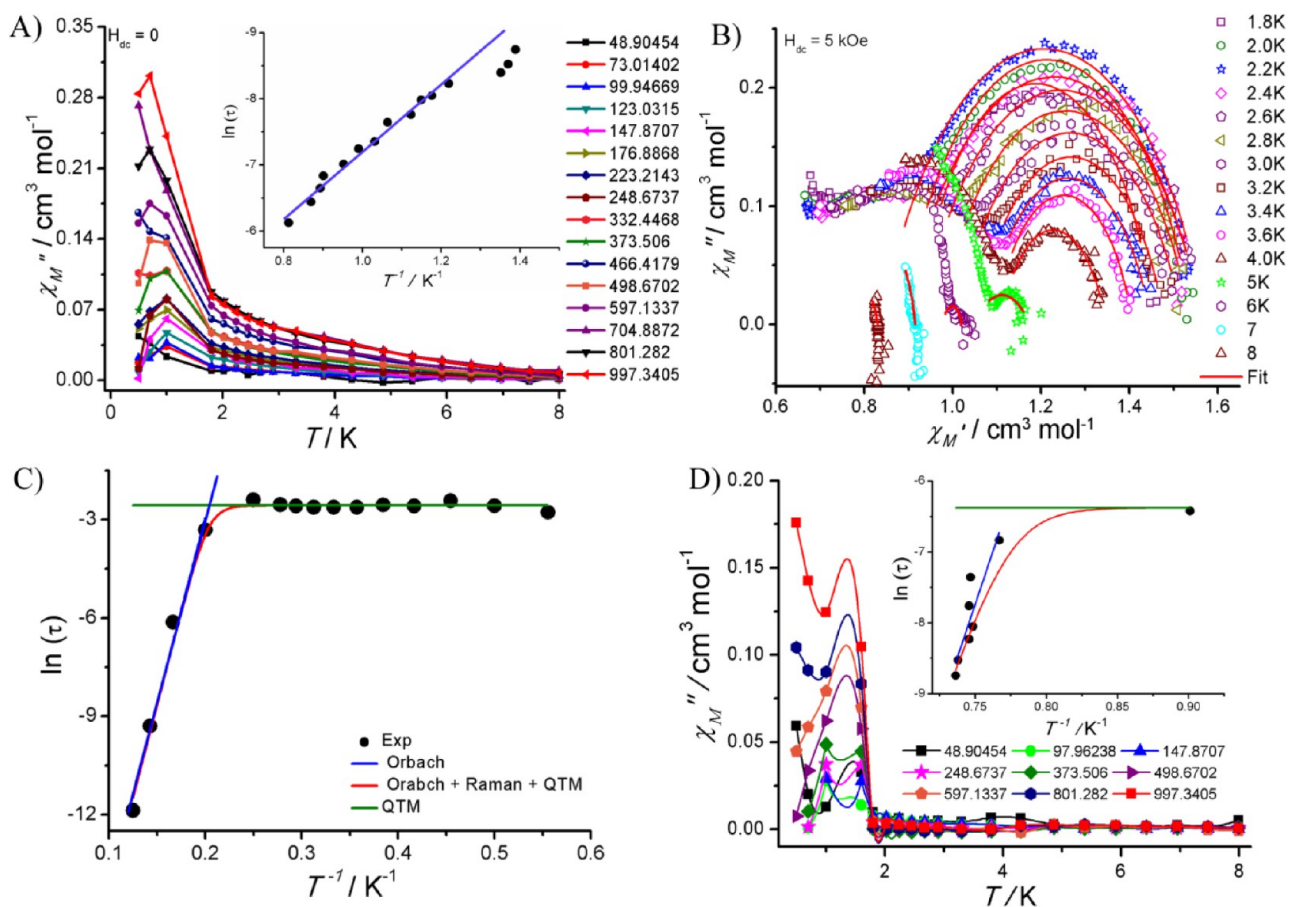
Figure 9. (A) Frequency-dependent out-of-phase susceptibility signal for complex **4** ($H_{dc} = 0$), Inset: Arrhenius plot constructed using the ac data of **4** measured under a zero bias field. (B) Cole−Cole plot for complex **4** ($H_{dc} = 5$ kOe). (C) Arrhenius plot of **4** constructed using the Cole−Cole fitting parameter (τ) measured in the presence of an external magnetic field of 5 kOe. The solid red traces in panels B and C represent the best fits obtained for the experimental data using the parameters described in the main text. (D) Frequency-dependent out-of-phase susceptibility signal for the diluted sample of **4** (50%, $H_{dc} = 0$). The inset in this panel represents the Arrhenius plot of the diluted samples, and the solid red line denotes the best fit obtained for the parameters described in the main text.

($C = 0.24$ s^{-1} K^{-n} and $n = 3.91$), and QTM ($\tau_{QTM} = 0.037$ s) processes (Figure 7F).

The unsuitable geometry around the Tb^{III} ion along with the integer spin nature of the m_j level is the likely reason for the absence of zero-field SIM, while slow relaxation of magnetization was induced by the application of an external magnetic field upon quenching of the faster relaxation such as QTM to some extent.

Magnetization relaxation measurements were performed on a polycrystalline sample of **3** in the presence of an external magnetic field of 3.5 kOe (Figure 8). Indeed **3** shows a χ_M'' signal indicative of the presence of slow relaxation of magnetization via a thermal energy barrier. Although the fast QTM relaxation was significantly suppressed, still more than one relaxation was operational, which is very well witnessed from Figure 8. The effective energy barrier for reorientation of the magnetization vector was estimated using eq 2, and the barrier height was found to be 44.07 cm^{-1} ($\tau_0 = 2.35 \times 10^{-9}$ s) including other relaxation processes such as Raman ($C = 0.056$ s^{-1} K^{-n} and $n = 4.08$) and QTM ($\tau_{QTM} = 0.0691$ s) (Figure 8E). The observation of slow relaxation of magnetization in **3** is often very rare because the complex possesses integer m_j levels at the ground state, where QTM is expected to be enormous. In addition, the presence of hyperfine interaction in the majority of the reported holmium(III) complexes (nuclear spin of

holmium = $^7/_2$) triggers fast relaxation within the m_j ground-state levels even in the presence of an applied bias field. The influence of hyperfine interaction on the magnetization relaxation dynamics in certain cobalt(II) complexes was very well witnessed by us in a recent report[6i] and in certain lanthanide complexes.[33] Only a very few holmium(III)-based field-induced SIMs are reported, and the energy barrier of **3** is comparable with those of other complexes reported in the literature.[1d,34]

In contrast to complexes **1**−**3**, complex **4** was found to show SIM behavior without the application of an external magnetic field in the temperature range between 1.8 and 8.0 K (Figure 9).

However, frequency-dependent χ_M'' signals were obtained without any well-resolved maxima. So, we recorded the magnetization relaxation dynamics below 1.8 K (up to 0.35 K) for complex **4** using a I-Helium3 setup, which was integrated with MPMS-XL (Figure 9). Well-resolved frequency-dependent χ_M'' signals were witnessed below 1.8 K, which suggests a zero-field SIM behavior of complex **4**. Such a zero-field SIM behavior for an unsymmetrical complex with point charge ligands such as HL and nitrates is extremely scarce in the literature, to the best of our knowledge.

From Figure 9A, it is very clear that there is another relaxation process operational at higher temperature (above 2
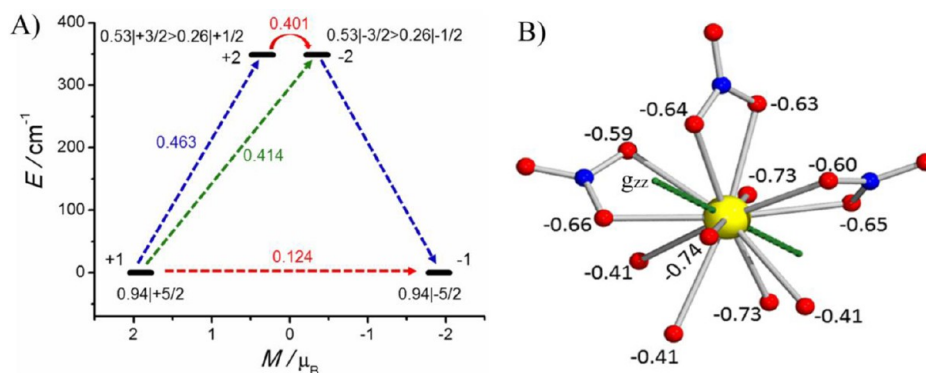
Figure 10. (A) Computed magnetization blocking barrier for complex **1**. Blue/green dotted lines represent the Orbach and Raman processes. Red dotted lines represent QTM/TA-QTM. The numbers provided at each arrow are the mean absolute values for the corresponding matrix element of the transition magnetic moment. (B) Orientation of the principle magnetization axis (g_{zz}) along with charge distribution on the coordinated atoms of **1** shown above.

K). However, the maxima in χ_M'' are not clearly visible for this relaxation process present at high temperature. To exclude the probability of magnetic phase transition at extremely low temperature, temperature-dependent heat capacity measurement was performed for complex **4** between 1.8 and 15 K (Figure S11). No λ-type anomaly was observed in this temperature range, which firmly supports that no magnetic phase transition occurs in complex **4**. The Arrhenius plot was constructed using the maxima observed in the $\chi_M''(T)$ plot and the effective energy barrier for the magnetization reversal estimated to be 3.61 cm^{-1}, which is very low. The small magnitude of the energy barrier for slow relaxation of magnetization is most likely due to the presence of multiple relaxation processes such as QTM. To suppress/quench QTM, we have repeated the ac magnetic susceptibility measurement in the presence of an external magnetic field (H_{dc} = 5 kOe; Figures 9B and S12). The Cole−Cole plot unambiguously confirms that more than one relaxation process is operational even in the presence of an external magnetic field (Figure 9B). Attempts were failed to fit the Cole−Cole plot considering more than one relaxation process. Hence, the major relaxation process was fitted to a generalized Debye model using eq 1 (Table S7). The Arrhenius plot was constructed using the relaxation time extracted from the Cole−Cole data fitting. Figure 9C evidently shows that above 3 K temperature dependent Orbach process is dominant, while below 3 K, magnetization of relaxation independent of the ac field signifies that QTM and/or other relaxation processes are dominant. Considering the multiple relaxation processes (as per eq 2), the Arrhenius curve was fitted over the entire temperature range. Excellent fits to the experimental data were obtained by incorporating Raman (C = 0.00046 s^{-1} K^{-n} and n = 5), Orbach (U_{eff} = 79.14 cm^{-1} and τ_0 = 6.77 × 10^{-12} s), and QTM (τ_{QTM} = 0.137 s) relaxation processes (Figure 9C).

Because complex **4** shows zero-field SIM behavior, in order to find out whether the observed slow relaxation of magnetization is of a molecular phenomenon or is due to magnetic ordering, we performed the magnetization of relaxation measurements for 5%, 10%, and 50% diluted samples of **4**. Magnetic dilution was performed using **5**, and the synthetic procedures for making various dilutions are detailed in the Experimental Methods section. Because χ_M'' signals observed in 5% and 10% samples are extremely noisy and weak (data not shown), relaxation measurement was performed on a 50% diluted sample. The diluted samples of **4** undoubtedly

demonstrate the presence of slow relaxation of magnetization at zero external magnetic field. The nonlinear Arrhenius experimental data were fitted using eq 2 with multiple relaxation processes such as Raman (C = 0.0056 s^{-1} K^{-n} and n = 5), Orbach (U_{eff} = 41.70 cm^{-1} and τ_0 = 1.245 × 10^{-23} s), and QTM (τ_{QTM} = 0.0017 s) (inset of Figure 9D). The barrier to the magnetization of relaxation was found to be increased by more than 10-fold (41.70 cm^{-1}) compared to its 100% sample of **4** (3.61 cm^{-1}). This experiment is evidently emphasizing that the magnetization of relaxation phenomenon is of molecular origin and the influence of dipolar interaction to the magnetization relaxation dynamics. The influence of dipolar interaction on the relaxation of magnetization dynamics was elegantly probed earlier by Meihaus and Long in other related SIMs or SMMs.[35]

Theoretical Studies of Complexes 1−4. As experimentally observed, complexes **1−3** show only field-induced SIM behavior, while **4** shows zero-field SIM behavior; to rationalize the difference observed in the relaxation of magnetization among a series of complexes isolated, ab initio calculations were performed on the crystal structures of complexes **1−4** using the MOLCAS suite.[18] The detailed methodology employed is discussed in the Materials and Methods section. Because the crystal lattice of complexes **2−4** contains two crystallographically distinct molecules (labeled as **n**a and **n**b, where n = 2, 3, or 4), calculations were performed on each geometrical isomer of these complexes, and the obtained results are discussed below.

The computed energy windows of all three Kramers doublets (KDs) for **1** span over 598 cm^{-1} (see Tables S8 and S9). The **g** tensors of the ground-state KDs for complex **1** (g_x = 0.064, g_y = 0.685, and g_z = 3.823) were found to be axial in nature but lack pure Ising nature, as is evident from the nonzero transverse component (Table S8). Wave-function analysis of **1** reveals that the ground-state KDs consist predominantly of $m_j = \langle \pm^5/_2|$ state. However, a small contribution from other states was noticed. Mixing of the m_j levels leads to large QTM between the ground states, as reflected in the computed values (see Figure 10A). This is consistent with the experimental observation that **1** does not show frequency-dependent out-of-phase susceptibility signals at zero dc magnetic field. Upon application of an optimum dc magnetic field, QTM is likely to be suppressed, and hence **1** was found to show field-induced SIM behavior. The easy-axis orientation of the magnetization vector computed for **1** along with charge distribution is shown
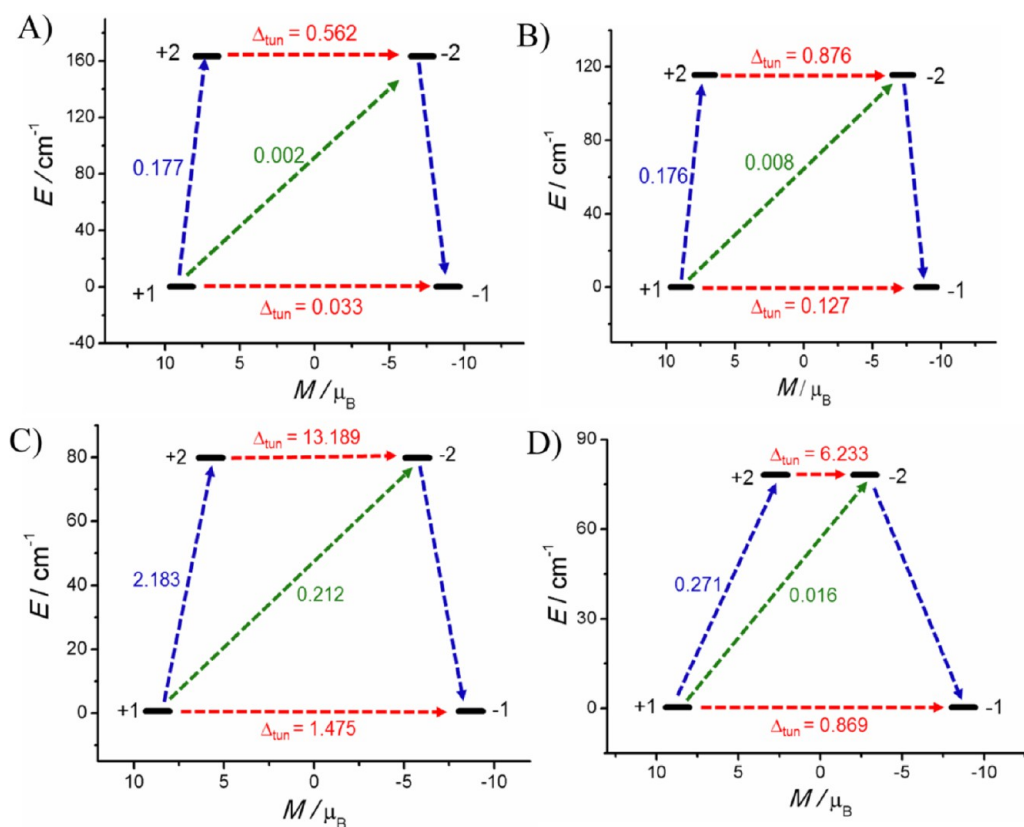
Figure 11. Computed magnetization blocking barrier for complexes (A) **2a**, (B) **2b**, (C) **3a**, and (D) **3b**. Blue/green dotted lines represent the Orbach and Raman processes. Red dotted lines represent the tunneling transitions within each doublet state.

in Figure 10B. The g_{zz} axis for the ground-state m_j level is located close to the phenoxo group of ligands with a tilt angle of 34° [g_{zz} axis−Ce−O51(phenoxo)]. The phenoxo O atoms contain the highest calculated charge (−0.74) among all of the coordinated atoms. The first excited KD ($g_x = 0.407$, $g_y = 1.567$, and $g_z = 3.202$) of **1** lies above 348 cm^{-1} from the ground-state KD, and its magnetization vector is tilted by 77° compared to the easy-axis orientation of its ground-state KD. The computed anisotropic energy barrier (348 cm^{-1}) is overestimated; however, the computed parameters unambiguously suggest that the magnetization vector relaxes via the first excited state, and the tentative mechanism of magnetization of relaxation is given in Figure 10A along with the possible relaxation processes and its transition probabilities. Such a large difference in the computed and experimental barrier heights was noted earlier for other reported cerium(III) SIMs.[30a]

To further understand the nature of the anisotropy, we have also computed crystal-field parameters for **1**. The corresponding crystal-field Hamiltonian can be given by eq 3, where B_k^q is the crystal-field parameter and $\tilde{O}_k^q$ is the Stevens operator.

$$\widehat{H}_{CF} = \sum_{k} \sum_{k=-q}^{q} B_k^q \tilde{O}_k^q \tag{3}$$

The ratio of the nonaxial term (B_k^q, where $q \neq 0$ and $k = 2$, 4, and 6) to the axial term (B_k^q, where $q = 0$ and $k = 2$, 4, and 6) found between 0.20 and 0.68 confirms that significant QTM is operational in **1** (see Table S9). Moreover, a very large value of B_2^0 (−26) indicates a prolate nature of the Ce^{III} ion, which is consistent with literature reports.[30a]

For complexes **2a** and **2b**, all of the $(2J + 1)$ m_j levels span in the energy windows of 518.3 and 394.8 cm^{-1}, respectively. In contrast to the electronic structure observed for **1**, the ground-state **g** tensors for complexes **2a** ($g_x = 0.00$, $g_y = 0.00$, and $g_z = 17.83$), **2b** ($g_x = 0.00$, $g_y = 0.00$, and $g_z = 17.87$), **3a** ($g_x = 0.00$, $g_y = 0.00$, and $g_z = 17.37$), and **3b** ($g_x = 0.00$, $g_y = 0.00$, and $g_z = 17.43$) are purely Ising in nature (Tables S10 and S11). The crystal-field parameters for complexes **2** and **3** were computed using eq 3 and are given in Table S12. For both complexes, the axial terms are higher in magnitude, which further confirms the Ising nature of the **g** tensors of the ground state. The magnitude of the B_2^0 parameter decreases in the same order as the decrease in the oblate character, −4.2 and −3.4 in the case of Tb^{III} and −0.86 and −0.70 in the case of Ho^{III} for **na** and **nb**, respectively (where $n = 2$ and **3**).[7,36] The energy gaps between the first excited state from the ground Ising state in **2a** and **2b** are found to be 162.9 and 115.4 cm^{-1}. The computed magnetic data [both $\chi_M T(T)$ and $M(H)$] using the parameters extracted from calculation are in excellent agreement with the experimental magnetic data, which reveals the reliability of the parameters extracted from the calculations (Figures 5 and S6). The ground-state tunneling gaps (Δ_{tun}) for both complexes (0.033 and 0.127 cm^{-1} for **2a** and **2b** and 1.475 and 0.869 cm^{-1} for **3a** and **3b**) were found to be very high, which indicates significant QTM via the ground-state m_j levels (Figure 11 and Tables S10 and S11).

This theoretical outcome strongly suggests that the frequency-dependent χ_M'' signal for these complexes at zero field is unlikely to be observed in the experiments. The application of an optimum external magnetic field lifts the degeneracy of the Ising doublets and, hence, quenches the

QTM to some extent. Thus, the field-induced magnetization behavior of complexes **2** and **3** can be observed. The effect of the orientation of the coordinating ligand along with the charge distribution on the coordinating atoms is clearly reflected in the magnetization easy axis of the ground-state Ising doublet in both isomers of complex **2** or **3** (Figure 12).
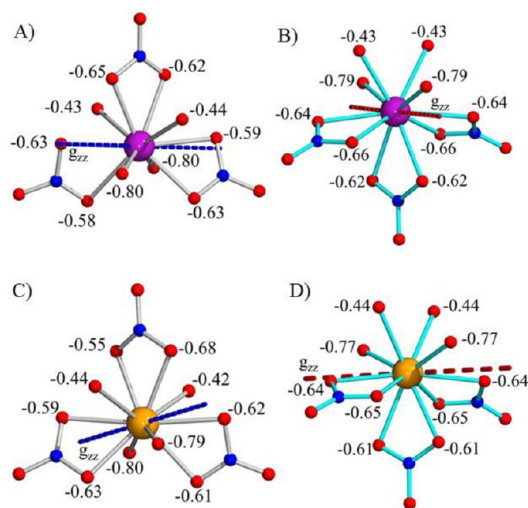
Figure 12. Picture representing the orientation of the principle magnetization axis (g_{zz}) along with the computed charge distribution on the coordinated atom for **2a** and **3a** (panels A and C) and **2b** and **3b** (panels B and D).

In both the **2a** and **2b** isomers, the orientation of the easy axis was found to be tilted toward the phenoxo O atom (Loprop charges −0.80 and −0.79) of the ligand by angles of 32° and 23°, respectively. This observation is consistent with the literature, where the orientation of the magnetization axis was found to be collinear with the atoms with high charge density.[37] This clearly emphasizes that both of these isomers in complex **2** are likely to have distinct relaxation behavior. The tunnel splitting values computed for the ground Ising state and first excited Ising state of both isomers (**2a** and **2b**) were found to be large in general; however, the **2b** tunnel splitting value was significantly larger than the value computed for **2a**. This rationalizes the observation of two different relaxation processes in the ac data collected at an optimum field of 5.5 kOe; i.e., a faster relaxation around 1000 Hz is likely due to the **2b** isomer because it possesses a large tunnel splitting value both in the ground and first excited Ising states compared to the **2a** isomers. To confirm this scenario unambiguously, one has to crystallize one of the isomers exclusively to be confident in the claim. However, we have not succeeded in our attempt to isolate the isomeric structures.

Because of the significant tunnel splitting in both **2a** and **2b** in the first excited Ising state, the magnetization vector is likely to relax via the first excited state, and the proposed mechanism along with various transition probabilities is shown in Figure 11. The computed anisotropic energy barriers are found to be 162.9 and 115.4 cm^{-1} for the **2a** and **2b** isomers, respectively. However, the experimentally observed energy barrier is significantly low (42 cm^{-1}). Smaller experimental U_{eff} values compared to the computed value can be understood by considering the other relaxation processes such as Raman and QTM, which are not taken into account in the ab initio calculated blockade barrier. In fact, the latter relaxation

processes are taken into consideration to fit the nonlinear part of the Arrhenius curve experimentally. The noticeable difference in the computed energy barrier and tunnel splitting values in the **2a** and **2b** isomers is due to the different orientations of the coordinating ligand to the central Tb(III) ion in **2**. For example, the ligand field in **2a** is more suitable for the oblate ion, which reflects a low Δ_{tun} of **2a** in comparison to **2b** (0.033 vs 0.127). This observation further confirms the better SMM behavior of **2a** in contrast to **2b**.

Unlike **2**, the energy gaps between the first excited and ground Ising states of **3a** and **3b** were computed to be 73.2 and 75.1 cm^{-1}, respectively (Figure 11). The tunnel splitting values of both the ground and excited Ising states of **3a**, however, are significantly larger than that of **3b**, which is actually reversed compared to the scenario in **2**. This consequence can be explained on the basis of the less oblate/more prolate nature of the Ho^{III} ion ground-state density. The ligand environment around the metal ion in **3b** is more suitable for a prolate ion. Hence, **3b** shows a slightly high anisotropic barrier with less tunneling gap, and conceivably molecule **3a** is likely to relax faster than **3b** at the optimum external magnetic field. This is further supported by the computed crystal-field parameters using eq 3. As mentioned earlier, the oblate nature of complex **3** (−0.86 and −0.70) decreases compared to that of **2** (−4.2 and −3.4); hence, the geometry around **3b** favors the prolate Ho^{III} ion. The computed Δ_{tun} (tunneling gap) for **3b** is found to be less compared to **3a**. This suggests that **3a** presumably relaxes faster than **3b**, and this scenario qualitatively can be visualized in ac relaxation measurements of **3**; i.e., Figure 8 evidently shows more than one relaxation process in the out-of-phase susceptibility data and Cole−Cole plot, which strongly corroborates the computational prediction. The orientation of the ground-state g_{zz} axis was found to tilt toward the phenoxo O atom (Loprop charges −0.80 vs −0.77) of the ligand by an angle of 25° in both molecules.

In contrast to complexes **1**-**3**, **4** shows zero-field SIM behavior. The ab initio calculations performed on the crystal structure of **4a** and **4b** clearly suggest that the **g** tensors of the ground-state KDs of **4a** (g_x = 1.03, g_y = 2.77, and g_z = 13.99) and **4b** (g_x = 0.04, g_y = 0.07, and g_z = 15.78) lack pure Ising nature while maintaining the axial signature with a significant nonzero transverse component in **4a** compared to **4b** (see Table S13). Wave-function analysis for both molecules (**4a** and **4b**) shows that that there is a strong mixing of the excited-state KD with the ground-state KD, but the major component comes from the $|\pm^{13}/_2\rangle$ state (Figure 13A). The computed **g** tensor of the ground-state KD clearly suggests that **4b** possesses an ideal ligand field compared to **4a**. The low symmetry observed in **4a** was further witnessed in the energy gap between the first ground- and excited-state KDs (49.6 cm^{-1}), compared to 105.9 cm^{-1} for **4b**. In complex **4**, because of low symmetry with a large transverse component in the ground-state KD of the **4a** isomer, the magnetization vector is expected to relax quickly preferably through QTM via the ground-state KD, while **4b** is envisaged to relax slower than **4a**.

Further, the ground-state g_{zz} orientation of **4a** is tilted by an angle of 96.4° compared to the ground-state g_{zz} orientation of **4b** (Figure 13). In **4a** and **4b**, the g_{zz} orientation of the first excited-state KD (g_x = 0.02, g_y = 3.22, and g_z = 11.30 for **4a** and g_x = 1.31, g_y = 5.10, and g_z = 12.34 for **4b**) tilted by an angle of 86.8° and 90° from its corresponding g_{zz} orientation of the ground-state KD. This suggests that the magnetization vector relaxes via the first excited state, and the computed energy
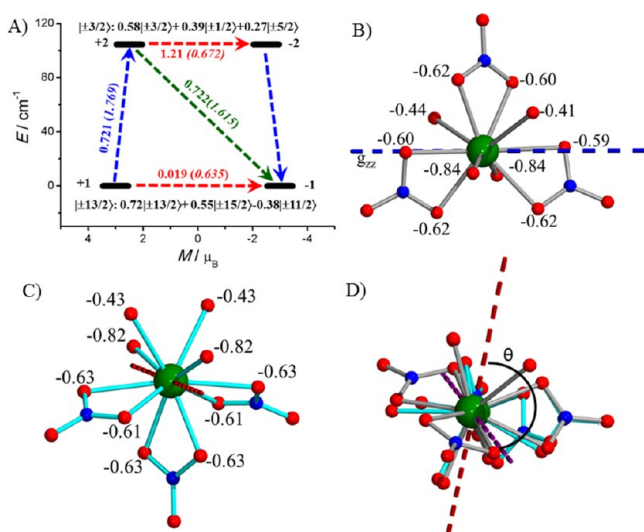
Figure 13. (A) Computed magnetization blocking barrier for complex **4b**. Numers in parentheses represent the corresponding values for **4a**. Blue/green dotted lines represent the Orbach and Raman processes. Red dotted lines represent QTM/TA-QTM. (B and C) Orientation of the principle magnetization axis (g_{zz}) along with the computed charge distribution on the coordinated atoms for complexes **4a** and **4b**, respectively. (D) **4a** and **4b** molecules overlayed on top of each other, as in the crystal lattice of **4**. θ represents the angle between the g_{zz} values of these structural isomers in the crystal lattice of **4** (see the main text for details).

barriers are observed to be 49.6 and 109.5 cm^{-1} for **4a** and **4b**, respectively. The calculations clearly propose that there must be more than one relaxation for these two isomers in **4**. As per these predictions, experimentally more than one relaxation process is observed both in the zero external magnetic field and in the presence of an optimum external magnetic field. There are no well-resolved maxima in the χ_M'' signal of **4** because of the presence of multiple relaxation processes; however, the existence of more than one relaxation process is unambiguously shown in the Cole−Cole plot (Figure 9).

To further probe the importance of the ligand field, calculations were performed on the model complexes (Figures S13 and S14 and Tables S15 and S16). The axial ligands were replaced systematically in complex **4a** with the molecular formulas [Er(HL)(NO$_3$)$_3$] (**4a-A**) and [Er(NO$_3$)$_3$] (**4a-B**), which results in a drastic increase of the anisotropic barrier from **4a** (3.6 cm^{-1}) to **4a-A** (78.1 cm^{-1}) to **4a-B** (133.4 cm^{-1}) (Tables S15 and S16).[15a] The studies performed on the model complexes evidently suggest that the presence of these axial ligands in complex **4** not only reduces the barrier height but also introduces significant transverse anisotropy, leading to an increase in QTM between the ground-state KDs.

CONCLUSION

In conclusion, we have isolated a series of mononuclear complexes with the molecular formulas [Ce(HL)$_3$(NO$_3$)$_3$] (**1**) and [Ln(HL)$_2$(NO$_3$)$_3$] [where Ln = Tb^{III} (**2**), Ho^{III} (**3**), Er^{III} (**4**), and Lu^{III} (**5**)], which are characterized by single-crystal XRD. Among all, complex **4** was found to show zero-field SMM behavior (3.61 cm^{-1}), although complexes **1−3** were noted as field-induced SMMs with the U_{eff} value of 26.06 cm^{-1} (H_{dc} = 3 kOe), 42 cm^{-1} (H_{dc} = 5.5 kOe), and 44.07 cm^{-1} (H_{dc} = 3.5 kOe), respectively. This has been rationalized through detailed computational calculations on these complexes, and a tentative

mechanism of relaxation for all of the complexes was computed. The computed magnetic data using the parameters extracted from the crystal structure of all of the complexes are in excellent agreement with the experimental magnetic data, suggesting the reliability of the parameters extracted. Overall, the calculations qualitatively predicts that the geometry around the **na** (where *n* = **2**, **3**, and **4**) molecule favors the oblate ion, while the geometry around the **nb** (where *n* = **2**, **3**, and **4**) isomer prefers a prolate. The calculations clearly reflect that, upon moving across the lanthanide series, the prolate nature of the Ln(III) ion becomes prominent, which is suitable for the ligand field provided by the HL ligand. The study presented in this Article contributes to the significance of the ligand field for isolating molecules with better SMM behavior.

ASSOCIATED CONTENT

ⓢ Supporting Information

The Supporting Information is available free of charge on the ACS Publications website at DOI: 10.1021/acs.inorgchem.7b02357.

> Powder XRD patterns, shape analyses, atoms involved in intermolecular hydrogen bonding, ball-and-stick representations, detailed magnetization, magnetization plots, field-sweep measurements, best-fitting parameters, heat capacity data, frequency-dependent out-of-phase susceptibility signals, computed **g** tensors and relative energies, crystal-field parameters, and orientation of **g** tensor of the ground-state KD for complex **4a-B** (PDF)

Accession Codes

CCDC 1571727−1571729 contain the supplementary crystallographic data for this paper. These data can be obtained free of charge via www.ccdc.cam.ac.uk/data_request/cif, or by emailing data_request@ccdc.cam.ac.uk, or by contacting The Cambridge Crystallographic Data Centre, 12 Union Road, Cambridge CB2 1EZ, UK; fax: +44 1223 336033.

AUTHOR INFORMATION

Corresponding Authors

*E-mail: rajaraman@chem.iitb.ac.in.
*E-mail: eswar@chem.iitb.ac.in. Tel: (+91)-22-2576-7187. Fax: (+91)-22-2576-7152.

ORCID ⓘ

Gopalan Rajaraman: 0000-0001-6133-3026
Maheswaran Shanmugam: 0000-0002-9012-743X

Notes

The authors declare no competing financial interest.

REFERENCES

(1) (a) Ishikawa, N.; Sugita, M.; Ishikawa, T.; Koshihara, S.-Y.; Kaizu, Y. Lanthanide Double-Decker Complexes Functioning as Magnets at the Single-Molecular Level. *J. Am. Chem. Soc.* **2003**, *125*, 8694−8695. (b) Liu, K.; Zhang, X.; Meng, X.; Shi, W.; Cheng, P.; Powell, A. K. Constraining the coordination geometries of lanthanide centers and magnetic building blocks in frameworks: a new strategy for molecular nanomagnets. *Chem. Soc. Rev.* **2016**, *45*, 2423−2439. (c) Ishikawa, N.;

Sugita, M.; Tanaka, N.; Ishikawa, T.; Koshihara, S.-Y.; Kaizu, Y. Upward Temperature Shift of the Intrinsic Phase Lag of the Magnetization of Bis(phthalocyaninato)terbium by Ligand Oxidation Creating an S = 1/2 Spin. *Inorg. Chem.* **2004**, *43*, 5498−5500. (d) Ishikawa, N.; Sugita, M.; Wernsdorfer, W. Nuclear Spin Driven Quantum Tunneling of Magnetization in a New Lanthanide Single-Molecule Magnet: Bis(Phthalocyaninato)holmium Anion. *J. Am. Chem. Soc.* **2005**, *127*, 3650−3651. (e) Takamatsu, S.; Ishikawa, T.; Koshihara, S.-y.; Ishikawa, N. Significant Increase of the Barrier Energy for Magnetization Reversal of a Single-4f-Ionic Single-Molecule Magnet by a Longitudinal Contraction of the Coordination Space. *Inorg. Chem.* **2007**, *46*, 7250−7252. (f) Woodruff, D. N.; Winpenny, R. E. P.; Layfield, R. A. Lanthanide single-molecule magnets. *Chem. Rev.* **2013**, *113*, 5110−5148. (g) Pointillart, F.; Cador, O.; Le Guennic, B.; Ouahab, L. Uncommon lanthanide ions in purely 4f Single Molecule Magnets. *Coord. Chem. Rev.* **2017**, *346*, 150−175. (h) Luzon, J.; Sessoli, R. Lanthanides in molecular magnetism: so fascinating, so challenging. *Dalton Trans.* **2012**, *41*, 13556−13567.

(2) (a) Candini, A.; Klyatskaya, S.; Ruben, M.; Wernsdorfer, W.; Affronte, M. Graphene Spintronic Devices with Molecular Nano-magnets. *Nano Lett.* **2011**, *11*, 2634−2639. (b) Lan, Y.; Klyatskaya, S.; Ruben, M. Bis(phthalocyaninato) lanthanide(III) complexes - from molecular magnetism to spintronic devices. *Lanthanides Actinides Mol. Magn.* **2015**, 223−292. (c) Schwoebel, J.; Fu, Y.; Brede, J.; Dilullo, A.; Hoffmann, G.; Klyatskaya, S.; Ruben, M.; Wiesendanger, R. Real-space observation of spin-split molecular orbitals of adsorbed single-molecule magnets. *Nat. Commun.* **2012**, *3*, 953. (d) Senthil Kumar, K.; Ruben, M. Emerging trends in spin crossover (SCO) based functional materials and devices. *Coord. Chem. Rev.* **2017**, *346*, 176−205.

(3) (a) Urdampilleta, M.; Klayatskaya, S.; Ruben, M.; Wernsdorfer, W. Magnetic Interaction Between a Radical Spin and a Single-Molecule Magnet in a Molecular Spin-Valve. *ACS Nano* **2015**, *9*, 4458−4464. (b) Urdampilleta, M.; Klyatskaya, S.; Cleuziou, J. P.; Ruben, M.; Wernsdorfer, W. Supramolecular spin valves. *Nat. Mater.* **2011**, *10*, 502−506.

(4) Sessoli, R.; Tsai, H. L.; Schake, A. R.; Wang, S.; Vincent, J. B.; Folting, K.; Gatteschi, D.; Christou, G.; Hendrickson, D. N. High-spin molecules: $[Mn_{12}O_{12}(O_2CR)_{16}(H_2O)_4]$. *J. Am. Chem. Soc.* **1993**, *115*, 1804−1816.

(5) (a) Boulon, M.-E.; Fernandez, A.; Moreno Pineda, E.; Chilton, N. F.; Timco, G.; Fielding, A. J.; Winpenny, R. E. P. Measuring Spin··· Spin Interactions between Heterospins in a Hybrid [2]Rotaxane. *Angew. Chem., Int. Ed.* **2017**, *56*, 3876−3879. (b) Ferrando-Soria, J.; Moreno Pineda, E.; Chiesa, A.; Fernandez, A.; Magee, S. A.; Carretta, S.; Santini, P.; Vitorica-Yrezabal, I. J.; Tuna, F.; Timco, G. A.; McInnes, E. J. L.; Winpenny, R. E. P. A modular design of molecular qubits to implement universal quantum gates. *Nat. Commun.* **2016**, *7*, 11377. (c) Ghirri, A.; Chiesa, A.; Carretta, S.; Troiani, F.; van Tol, J.; Hill, S.; Vitorica-Yrezabal, I.; Timco, G. A.; Winpenny, R. E. P.; Affronte, M. Coherent Spin Dynamics in Molecular Cr_8Zn Wheels. *J. Phys. Chem. Lett.* **2015**, *6*, 5062−5066. (d) Timco, G. A.; Carretta, S.; Troiani, F.; Tuna, F.; Pritchard, R. J.; Muryn, C. A.; McInnes, E. J. L.; Ghirri, A.; Candini, A.; Santini, P.; Amoretti, G.; Affronte, M.; Winpenny, R. E. P. Engineering the coupling between molecular spin qubits by coordination chemistry. *Nat. Nanotechnol.* **2009**, *4*, 173−178. (e) Wedge, C. J.; Timco, G. A.; Spielberg, E. T.; George, R. E.; Tuna, F.; Rigby, S.; McInnes, E. J. L.; Winpenny, R. E. P.; Blundell, S. J.; Ardavan, A. Chemical engineering of molecular qubits. *Phys. Rev. Lett.* **2012**, *108*, 107201.

(6) (a) Bao, S.-S.; Zheng, L.-M. Magnetic materials based on 3d metal phosphonates. *Coord. Chem. Rev.* **2016**, *319*, 63−85. (b) Craig, G. A.; Murrie, M. 3d single-ion magnets. *Chem. Soc. Rev.* **2015**, *44*, 2135−2147. (c) DeGayner, J. A.; Jeon, I.-R.; Harris, T. D. A series of tetraazalene radical-bridged M_2 (M = CrIII, MnII, FeII, CoII) complexes with strong magnetic exchange coupling. *Chem. Sci.* **2015**, *6*, 6639−6648. (d) Frost, J. M.; Harriman, K. L. M.; Murugesu, M. The rise of 3-d single-ion magnets in molecular magnetism: towards materials from molecules? *Chem. Sci.* **2016**, *7*, 2470−2491.

(e) Novikov, V. V.; Pavlov, A. A.; Nelyubina, Y. V.; Boulon, M.-E.; Varzatskii, O. A.; Voloshin, Y. Z.; Winpenny, R. E. P. A Trigonal Prismatic Mononuclear Cobalt(II) Complex Showing Single-Molecule Magnet Behavior. *J. Am. Chem. Soc.* **2015**, *137*, 9792−9795. (f) Baskar, V.; Shanmugam, M.; Sanudo, E. C.; Shanmugam, M.; Collison, D.; McInnes, E. J. L.; Wei, Q.; Winpenny, R. E. P. Metal cages using a bulky phosphonate as a ligand. *Chem. Commun.* **2007**, 37−39. (g) Shanmugam, M.; Chastanet, G.; Mallah, T.; Sessoli, R.; Teat, S. J.; Timco, G. A.; Winpenny, R. E. P. Synthesis and characterization of mixed-valent manganese phosphonate cage complexes. *Chem. - Eur. J.* **2006**, *12*, 8777−8785. (h) Vaidya, S.; Singh, S. K.; Shukla, P.; Ansari, K.; Rajaraman, G.; Shanmugam, M. Role of Halide Ions in the Nature of the Magnetic Anisotropy in Tetrahedral CoII Complexes. *Chem. - Eur. J.* **2017**, *23*, 9546−9559. (i) Vaidya, S.; Tewary, S.; Singh, S. K.; Langley, S. K.; Murray, K. S.; Lan, Y.; Wernsdorfer, W.; Rajaraman, G.; Shanmugam, M. What Controls the Sign and Magnitude of Magnetic Anisotropy in Tetrahedral Cobalt(II) Single-Ion Magnets? *Inorg. Chem.* **2016**, *55*, 9564−9578. (j) Vaidya, S.; Upadhyay, A.; Singh, S. K.; Gupta, T.; Tewary, S.; Langley, S. K.; Walsh, J. P. S.; Murray, K. S.; Rajaraman, G.; Shanmugam, M. A synthetic strategy for switching the single ion anisotropy in tetrahedral Co(II) complexes. *Chem. Commun.* **2015**, *51*, 3739−3742. (k) Aromi, G.; Brechin, E. K. Synthesis of 3d metallic single-molecule magnets. *Struct. Bonding (Berlin, Ger.)* **2006**, *122*, 1−67.

(7) Rinehart, J. D.; Long, J. R. Exploiting single-ion anisotropy in the design of f-element single-molecule magnets. *Chem. Sci.* **2011**, *2*, 2078−2085.

(8) (a) Bag, P.; Rastogi, C. K.; Biswas, S.; Sivakumar, S.; Mereacre, V.; Chandrasekhar, V. Homodinuclear lanthanide $\{Ln_2\}$ (Ln = Gd, Tb, Dy, Eu) complexes prepared from an o-vanillin based ligand: luminescence and single-molecule magnetism behavior. *Dalton Trans.* **2015**, *44*, 4328−4340. (b) Biswas, S.; Das, S.; van Leusen, J.; Koegerler, P.; Chandrasekhar, V. Tetranuclear [2 × 2] Square-Grid Lanthanide(III) Complexes: Syntheses, Structures, and Magnetic Properties. *Eur. J. Inorg. Chem.* **2014**, *2014*, 4159−4167. (c) Das, S.; Dey, A.; Biswas, S.; Colacio, E.; Chandrasekhar, V. Hydroxide-Free Cubane-Shaped Tetranuclear $[Ln_4]$ Complexes. *Inorg. Chem.* **2014**, *53*, 3417−3426. (d) Das, S.; Hossain, S.; Dey, A.; Biswas, S.; Sutter, J.-P.; Chandrasekhar, V. Molecular Magnets Based on Homometallic Hexanuclear Lanthanide(III) Complexes. *Inorg. Chem.* **2014**, *53*, 5020−5028. (e) Demir, S.; Nippe, M.; Gonzalez, M. I.; Long, J. R. Exchange coupling and magnetic blocking in dilanthanide complexes bridged by the multi-electron redox-active ligand 2,3,5,6-tetra(2-pyridyl) pyrazine. *Chem. Sci.* **2014**, *5*, 4701−4711. (f) Demir, S.; Zadrozny, J. M.; Long, J. R. Large Spin-Relaxation Barriers for the Low-Symmetry Organolanthanide Complexes $[Cp*_2Ln(BPh_4)]$ (Cp*=pentamethylcyclopentadienyl; Ln = Tb, Dy). *Chem. - Eur. J.* **2014**, *20*, 9524−9529. (g) Guo, P.-H.; Meng, Y.; Chen, Y.-C.; Li, Q.-W.; Wang, B.-Y.; Leng, J.-D.; Bao, D.-H.; Jia, J.-H.; Tong, M.-L. A zigzag DyIII4 cluster exhibiting single-molecule magnet, ferroelectric and white-light emitting properties. *J. Mater. Chem. C* **2014**, *2*, 8858−8864. (h) Gupta, T.; Rajaraman, G. How strongly are the magnetic anisotropy and coordination numbers correlated in lanthanide based molecular magnets. *J. Chem. Sci.* **2014**, *126*, 1569−1579. (i) Huang, W.; Le Roy, J. J.; Khan, S. I.; Ungur, L.; Murugesu, M.; Diaconescu, P. L. Tetraanionic Biphenyl Lanthanide Complexes as Single-Molecule Magnets. *Inorg. Chem.* **2015**, *54*, 2374−2382. (j) Li, L.-L.; Liu, S.; Zhang, Y.; Shi, W.; Cheng, P. Three new mononuclear tri-spin lanthanide-nitronyl nitroxide radical compounds: syntheses, structures and magnetic properties. *Dalton Trans.* **2015**, *44*, 6118−6125. (k) Luan, F.; Yan, P.; Zhu, J.; Liu, T.; Zou, X.; Li, G. A salen-type Dy_4 single-molecule magnet with an enhanced energy barrier and its analogues. *Dalton Trans.* **2015**, *44*, 4046−4053. (l) Marx, R.; Moro, F.; Doerfel, M.; Ungur, L.; Waters, M.; Jiang, S. D.; Orlita, M.; Taylor, J.; Frey, W.; Chibotaru, L. F.; van Slageren, J. Spectroscopic determination of crystal field splittings in lanthanide double deckers. *Chem. Sci.* **2014**, *5*, 3287−3293. (m) Moreno Pineda, E.; Chilton, N. F.; Marx, R.; Dorfel, M.; Sells, D. O.; Neugebauer, P.; Jiang, S.-D.; Collison, D.; van Slageren, J.; McInnes, E. J. L.; Winpenny, R. E. P.

Direct measurement of dysprosium(III) dysprosium(III) interactions in a single-molecule magnet. *Nat. Commun.* **2014**, *5*, 5243. (n) Singh, S. K.; Gupta, T.; Rajaraman, G. Magnetic Anisotropy and Mechanism of Magnetic Relaxation in Er(III) Single-Ion Magnets. *Inorg. Chem.* **2014**, *53*, 10835−10845. (o) Singh, S. K.; Gupta, T.; Shanmugam, M.; Rajaraman, G. Unprecedented magnetic relaxation via the fourth excited state in low-coordinate lanthanide single-ion magnets. A theoretical perspective. *Chem. Commun.* **2014**, *50*, 15513−15516. (p) Ungur, L.; Lin, S.-Y.; Tang, J.; Chibotaru, L. F. Single-molecule toroics in Ising-type lanthanide molecular clusters. *Chem. Soc. Rev.* **2014**, *43*, 6894−6905. (q) Zhang, P.; Zhang, L.; Tang, J. Lanthanide single molecule magnets: progress and perspective. *Dalton Trans.* **2015**, *44*, 3923−3929. (r) Zou, H.-H.; Sheng, L.-B.; Chen, Z.-L.; Liang, F.-P. Lanthanide nonanuclear clusters with sandglass-like topology and the SMM behavior of dysprosium analogue. *Polyhedron* **2015**, *88*, 110−115.

(9) Sessoli, R.; Boulon, M.-E.; Caneschi, A.; Mannini, M.; Poggini, L.; Wilhelm, F.; Rogalev, A. Strong magneto-chiral dichroism in a paramagnetic molecular helix observed by hard X-rays. *Nat. Phys.* **2014**, *11*, 69−74.

(10) (a) Rinehart, J. D.; Fang, M.; Evans, W. J.; Long, J. R. A N_2^{3-} Radical-Bridged Terbium Complex Exhibiting Magnetic Hysteresis at 14 K. *J. Am. Chem. Soc.* **2011**, *133*, 14236−14239. (b) Harriman, K. L. M.; Brosmer, J. L.; Ungur, L.; Diaconescu, P. L.; Murugesu, M. Pursuit of Record Breaking Energy Barriers: A Study of Magnetic Axiality in Diamide Ligated DyIII Single-Molecule Magnets. *J. Am. Chem. Soc.* **2017**, *139*, 1420−1423. (c) Guo, F.-S.; Day, B. M.; Chen, Y.-C.; Tong, M.-L.; Mansikkamaeki, A.; Layfield, R. A. A Dysprosium Metallocene Single-Molecule Magnet Functioning at the Axial Limit. *Angew. Chem., Int. Ed.* **2017**, *56*, 11445−11449. (d) Goodwin, C. A. P.; Ortu, F.; Reta, D.; Chilton, N. F.; Mills, D. P. Molecular magnetic hysteresis at 60 K in dysprosocenium. *Nature* **2017**, *548*, 439−442. (e) Liu, J.; Chen, Y.-C.; Liu, J.-L.; Vieru, V.; Ungur, L.; Jia, J.-H.; Chibotaru, L. F.; Lan, Y.; Wernsdorfer, W.; Gao, S.; Chen, X.-M.; Tong, M.-L. A Stable Pentagonal Bipyramidal Dy(III) Single-Ion Magnet with a Record Magnetization Reversal Barrier over 1000 K. *J. Am. Chem. Soc.* **2016**, *138*, 5441−5450. (f) Gupta, S. K.; Rajeshkumar, T.; Rajaraman, G.; Murugavel, R. An air-stable Dy(III) single-ion magnet with high anisotropy barrier and blocking temperature. *Chem. Sci.* **2016**, *7*, 5181−5191.

(11) (a) Maheswaran, S.; Chastanet, G.; Teat, S. J.; Mallah, T.; Sessoli, R.; Wernsdorfer, W.; Winpenny, R. E. P. Phosphonate ligands stabilize mixed-valent {MnIII20-xMnIIx} clusters with large spin and coercivity. *Angew. Chem., Int. Ed.* **2005**, *44*, 5044−5048. (b) Ako, A. M.; Hewitt, I. J.; Mereacre, V.; Clerac, R.; Wernsdorfer, W.; Anson, C. E.; Powell, A. K. A ferromagnetically coupled Mn₁₉ aggregate with a record S = 83/2 ground spin state. *Angew. Chem., Int. Ed.* **2006**, *45*, 4926−4929. (c) Milios, C. J.; Inglis, R.; Vinslava, A.; Bagai, R.; Wernsdorfer, W.; Parsons, S.; Perlepes, S. P.; Christou, G.; Brechin, E. K. Toward a Magnetostructural Correlation for a Family of Mn₆ SMMs. *J. Am. Chem. Soc.* **2007**, *129*, 12505−12511. (d) Upadhyay, A.; Rajpurohit, J.; Kumar Singh, M.; Dubey, R.; Kumar Srivastava, A.; Kumar, A.; Rajaraman, G.; Shanmugam, M. Hydroxo-Bridged Dimers of Oxo-Centered Ruthenium(III) Triangle: Synthesis and Spectroscopic and Theoretical Investigations. *Chem. - Eur. J.* **2014**, *20*, 6061−6070.

(12) Gatteschi, D.; Sessoli, R. Quantum tunneling of magnetization and related phenomena in molecular materials. *Angew. Chem., Int. Ed.* **2003**, *42*, 268−297.

(13) Le Roy, J. J.; Ungur, L.; Korobkov, I.; Chibotaru, L. F.; Murugesu, M. Coupling strategies to enhance single-molecule magnet properties of erbium-cyclooctatetraenyl complexes. *J. Am. Chem. Soc.* **2014**, *136*, 8003−8010.

(14) Liu, F.; Krylov, D. S.; Spree, L.; Avdoshenko, S. M.; Samoylova, N. A.; Rosenkranz, M.; Kostanyan, A.; Greber, T.; Wolter, A. U. B.; Buechner, B.; Popov, A. A. Single molecule magnet with an unpaired electron trapped between two lanthanide ions inside a fullerene. *Nat. Commun.* **2017**, *8*, 16098.

(15) (a) Das, C.; Upadhyay, A.; Vaidya, S.; Singh, S. K.; Rajaraman, G.; Shanmugam, M. Origin of SMM behaviour in an asymmetric Er(III) Schiff base complex: a combined experimental and theoretical study. *Chem. Commun.* **2015**, *51*, 6137−6140. (b) Ishikawa, N. Phthalocyanine-based magnets. *Struct. Bonding (Berlin, Ger.)* **2010**, *135*, 211−228.

(16) (a) Upadhyay, A.; Das, C.; Vaidya, S.; Singh, S. K.; Gupta, T.; Mondol, R.; Langley, S. K.; Murray, K. S.; Rajaraman, G.; Shanmugam, M. Role of the Diamagnetic Zinc(II) Ion in Determining the Electronic Structure of Lanthanide Single-Ion Magnets. *Chem. - Eur. J.* **2017**, *23*, 4903−4916. (b) Upadhyay, A.; Singh, S. K.; Das, C.; Mondol, R.; Langley, S. K.; Murray, K. S.; Rajaraman, G.; Shanmugam, M. Enhancing the effective energy barrier of a Dy(III) SMM using a bridged diamagnetic Zn(II) ion. *Chem. Commun.* **2014**, *50*, 8838−8841.

(17) (a) Yeap, G.-Y.; Ha, S.-T.; Ishizawa, N.; Suda, K.; Boey, P.-L.; Kamil Mahmood, W. A. Synthesis, crystal structure and spectroscopic study of para substituted 2-hydroxy-3-methoxybenzylideneanilines. *J. Mol. Struct.* **2003**, *658*, 87−99. (b) Upadhyay, A.; Vaidya, S.; Venkatasai, V. S.; Jayapal, P.; Srivastava, A. K.; Shanmugam, M.; Shanmugam, M. Synthesis and characterization of 3d and 4f metal complexes of Schiff base ligands. *Polyhedron* **2013**, *66*, 87−96.

(18) Aquilante, F.; Autschbach, J.; Carlson, R. K.; Chibotaru, L. F.; Delcey, M. G.; De Vico, L.; Galván, F. I.; Ferre, N.; Frutos, L. M.; Gagliardi, L.; et al. MOLCAS 8: New Capabilities for Multiconfigurational Quantum Chemical Calculations across the Periodic Table. *J. Comput. Chem.* **2016**, *37*, 506−541.

(19) Hess, B. A.; Marian, C. M.; Wahlgren, U.; Gropen, O. A mean-field spin-orbit method applicable to correlated wavefunctions. *Chem. Phys. Lett.* **1996**, *251*, 365−371.

(20) Roos, B. O.; Malmqvist, P.-A. Relativistic quantum chemistry: the multiconfigurational approach. *Phys. Chem. Chem. Phys.* **2004**, *6*, 2919−2927.

(21) Roos, B. O.; Lindh, R.; Malmqvist, P.; Veryazov, V.; Widmark, P.-O.; Borin, A. C. New Relativistic Atomic Natural Orbital Basis Sets for Lanthanide Atoms with Applications to the Ce Diatom and LuF₃. *J. Phys. Chem. A* **2008**, *112*, 11431−11435.

(22) Malmqvist, P. A.; Roos, B. O.; Schimmelpfennig, B. The restricted active space (RAS) state interaction approach with spin-orbit coupling. *Chem. Phys. Lett.* **2002**, *357*, 230−240.

(23) Chibotaru, L. F.; Ungur, L. *Ab initio* calculation of anisotropic magnetic properties of complexes. I. Unique definition of pseudo spin Hamiltonians and their derivation. *J. Chem. Phys.* **2012**, *137*, 064112.

(24) Pinsky, M.; Avnir, D. Continuous Symmetry Measures. 5. The Classical Polyhedra. *Inorg. Chem.* **1998**, *37*, 5575−5582.

(25) Lee, J. D. *Concise Inorganic Chemistry*; Blackwell Science Ltd., 1996; p 861.

(26) Langley, S. K.; Chilton, N. F.; Ungur, L.; Moubaraki, B.; Chibotaru, L. F.; Murray, K. S. Heterometallic Tetranuclear [LnIII₂CoIII₂] Complexes Including Suppression of Quantum Tunneling of Magnetization in the [DyIII₂CoIII₂] Single Molecule Magnet. *Inorg. Chem.* **2012**, *51*, 11873−11881.

(27) (a) Costes, J.-P.; Dahan, F.; Nicodeme, F. Structure-Based Description of a Step-by-Step Synthesis of Homo- and Hetero-dinuclear (4f, 4f′) Lanthanide Complexes. *Inorg. Chem.* **2003**, *42*, 6556−6563. (b) Corrigan, M. F.; Rae, I. D.; West, B. O. The constitution of N-substituted 2-(iminomethyl)benzenethiols (o-mercaptobenzaldimines). *Aust. J. Chem.* **1978**, *31*, 587−594.

(28) Upadhyay, A.; Das, C.; Shanmugam, M.; Langley, S. K.; Murray, K. S.; Shanmugam, M. Electronic and Magnetic Properties of a Gadolinium(III) Schiff Base Complex. *Eur. J. Inorg. Chem.* **2014**, *2014*, 4320−4325.

(29) (a) Zhang, P.; Guo, Y.-N.; Tang, J. Recent advances in dysprosium-based single molecule magnets: Structural overview and synthetic strategies. *Coord. Chem. Rev.* **2013**, *257*, 1728−1763. (b) Chilton, N. F.; Langley, S. K.; Moubaraki, B.; Soncini, A.; Batten, S. R.; Murray, K. S. Single molecule magnetism in a family of mononuclear β-diketonate lanthanide(III) complexes. Rationalization

of magnetic anisotropy in complexes of low symmetry. *Chem. Sci.* **2013**, *4*, 1719−1730.

(30) (a) Singh, S. K.; Gupta, T.; Ungur, L.; Rajaraman, G. Magnetic Relaxation in Single-Electron Single-Ion Cerium(III) Magnets: Insights from *Ab Initio* Calculations. *Chem. - Eur. J.* **2015**, *21*, 13812−13819. (b) Wada, H.; Ooka, S.; Yamamura, T.; Kajiwara, T. Light Lanthanide Complexes with Crown Ether and Its Aza Derivative Which Show Slow Magnetic Relaxation Behaviors. *Inorg. Chem.* **2017**, *56*, 147−155. (c) Khelifa, A. B.; Belkhiria, M. S.; Huang, G.; Freslon, S.; Guillou, O.; Bernot, K. Single-molecule magnet behaviour in polynuclear assembly of trivalent cerium ions with polyoxomolybdates. *Dalton Trans.* **2015**, *44*, 16458−16464. (d) Hino, S.; Maeda, M.; Kataoka, Y.; Nakano, M.; Yamamura, T.; Kajiwara, T. SMM behavior observed in $Ce(III)Zn(II)_2$ linear trinuclear complex. *Chem. Lett.* **2013**, *42*, 1276−1278. (e) Hino, S.; Maeda, M.; Yamashita, K.; Kataoka, Y.; Nakano, M.; Yamamura, T.; Nojiri, H.; Kofu, M.; Yamamuro, O.; Kajiwara, T. Linear trinuclear Zn(II)-Ce(III)-Zn(II) complex which behaves as a single-molecule magnet. *Dalton Trans.* **2013**, *42*, 2683−2686.

(31) Lucaccini, E.; Sorace, L.; Perfetti, M.; Costes, J.-P.; Sessoli, R. Beyond the anisotropy barrier: slow relaxation of the magnetization in both easy-axis and easy-plane Ln(trensal) complexes. *Chem. Commun.* **2014**, *50*, 1648−1651.

(32) (a) Boulon, M.-E.; Cucinotta, G.; Luzon, J.; Degl'Innocenti, C.; Perfetti, M.; Bernot, K.; Calvez, G.; Caneschi, A.; Sessoli, R. Magnetic anisotropy and spin-parity effect along the series of lanthanide complexes with DOTA. *Angew. Chem., Int. Ed.* **2013**, *52*, 350−354. (b) Cucinotta, G.; Perfetti, M.; Luzon, J.; Etienne, M.; Car, P.-E.; Caneschi, A.; Calvez, G.; Bernot, K.; Sessoli, R. Magnetic Anisotropy in a Dysprosium/DOTA Single-Molecule Magnet: Beyond Simple Magneto-Structural Correlations. *Angew. Chem., Int. Ed.* **2012**, *51* (7), 1606.

(33) (a) Shiddiq, M.; Komijani, D.; Duan, Y.; Gaita-Arino, A.; Coronado, E.; Hill, S. Enhancing coherence in molecular spin qubits via atomic clock transitions. *Nature* **2016**, *531*, 348−351. (b) Baldovi, J. J.; Duan, Y.; Bustos, C.; Cardona-Serra, S.; Gouzerh, P.; Villanneau, R.; Gontard, G.; Clemente-Juan, J. M.; Gaita-Arino, A.; Gimenez-Saiz, C.; Proust, A.; Coronado, E. Single ion magnets based on lanthanoid polyoxomolybdate complexes. *Dalton Trans.* **2016**, *45*, 16653−16660. (c) Giansiracusa, M. J.; Vonci, M.; Van den Heuvel, W.; Gable, R. W.; Moubaraki, B.; Murray, K. S.; Yu, D.; Mole, R. A.; Soncini, A.; Boskovic, C. Carbonate-Bridged Lanthanoid Triangles: Single-Molecule Magnet Behavior, Inelastic Neutron Scattering, and Ab Initio Studies. *Inorg. Chem.* **2016**, *55*, 5201−5214.

(34) (a) AlDamen, M. A.; Clemente-Juan, J. M.; Coronado, E.; Marti-Gastaldo, C.; Gaita-Arino, A. Mononuclear Lanthanide Single-Molecule Magnets Based on Polyoxometalates. *J. Am. Chem. Soc.* **2008**, *130*, 8874−8875. (b) Chen, Y.-C.; Liu, J.-L.; Chen, X.-M.; Tong, M.-L.; Wernsdorfer, W.; Liu, D.; Chibotaru, F. Hyperfine-Interaction-Driven Suppression of Quantum Tunneling at Zero Field in a Holmium(III) Single-Ion Magnet. *Angew. Chem., Int. Ed.* **2017**, *56*, 4996−5000. (c) Jiang, S.-D.; Liu, S.-S.; Zhou, L.-N.; Wang, B.-W.; Wang, Z.-M.; Gao, S. Series of Lanthanide Organometallic Single-Ion Magnets. *Inorg. Chem.* **2012**, *51*, 3079−3087. (d) Kajiwara, T. A Holmium(III)-Based Single-Molecule Magnet with Pentagonal-Bipyramidal Geometry. *Angew. Chem., Int. Ed.* **2017**, *56*, 11306−11308.

(35) Meihaus, K. R.; Long, J. R. Magnetic Blocking at 10 K and a Dipolar-Mediated Avalanche in Salts of the Bis(η^8-cyclooctatetraenide) Complex $[Er(COT)_2]$. *J. Am. Chem. Soc.* **2013**, *135*, 17952−17957.

(36) Gupta, T.; Velmurugan, G.; Rajeshkumar, T.; Rajaraman, G. Role of Lanthanide-Ligand bonding in the magnetization relaxation of mononuclear single-ion magnets: A case study on Pyrazole and Carbene ligated LnIII(Ln = Tb, Dy, Ho, Er) complexes. *J. Chem. Sci.* **2016**, *128*, 1615−1630.

(37) Chilton, N. F.; Collison, D.; McInnes, E. J. L.; Winpenny, R. E. P.; Soncini, A. An electrostatic model for the determination of magnetic anisotropy in dysprosium complexes. *Nat. Commun.* **2013**, *4*, 3551−3557.